Source Sector and Region Contributions to BC and $PM_{2.5}$ in Central Asia

S. Kulkarni[1*], N. Sobhani[1,2], J. P. Miller-Schulze[3,4], M. M. Shafer[3,4,], J. J. Schauer[3,4], P. A. Solomon[5], P. E. Saide[1], S. N. Spak[6,1], Y. F. Cheng[1**], H.A.C. Denier van der Gon[7], Z. Lu[8], D.G. Streets[8], G. Janssens-Maenhout[9], C. Wiedinmyer[10], J. Lantz[11], M. Artamonova[12], B. Chen[13], S. Imashev[13], L. Sverdlik[13], J. T. Deminter[3], B. Adhikary[1***], A. D'Allura[14], C. Wei[1****], and G. R. Carmichael[1,2]

[1]Center for Global and Regional Environmental Research, University of Iowa, Iowa City, IA

[2]Department of Chemical & Biochemical Engineering, The University of Iowa, Iowa City, IA 52242, USA

[3] Wisconsin State Laboratory of Hygiene, 2601 Agriculture Drive, Madison, WI 53718, USA

[4] Environmental Chemistry and Technology Program, 660 North Park St, University of Wisconsin, Madison, WI 53706, USA

[5] U.S. EPA, Office of Research & Development, Las Vegas, NV 89193, USA

[6] Public Policy Center, University of Iowa, 223 South Quadrangle, Iowa City, IA 52242

[7] TNO, Princetonlaan 6, 3584 CB Utrecht, The Netherlands

[8]Decision and Information Sciences Division, Argonne National Laboratory, Argonne, IL, USA

[9]European Commission, Joint Research Centre, IES, 21027 Ispra, Italy

[10]National Center for Atmospheric Research, Boulder, Colorado, USA

[11] U.S. EPA, Office of Radiation and Indoor Air, Las Vegas, NV 89193, USA

[12] Institute of Atmospheric Physics, 109017 Moscow, Russia

[13] Kyrgyz-Russian Slavic University, 44 Kievskaya Str., Bishkek 720000, Kyrgyzstan

[14]ARIANET, via Gilino 9, 20128 Milan, Italy

[*] now at: California Air Resource Board, Sacramento, CA USA

**now at: Multiphase chemistry department, Max Planck Institute for Chemistry, Mainz 55128, Germany

*** now at: International Centre for Integrated Mountain Development (ICIMOD), GPO Box 3226, Kathmandu, Nepal

****now at US EPA, Atmospheric Modeling and Analysis Division, Research Triangle Park, NC USA

Correspondence to: N. Sobhani (negin-sobhani@uiowa.edu) and G.R. Carmichael (gcarmich@engineering.uiowa.edu)

Abstract

Particulate matter (PM) mass concentrations, seasonal cycles, source sector and source region contributions in Central Asia (CA) are analyzed for the period April 2008-July 2009 using the Sulfur Transport and dEposition Model (STEM) chemical transport model and modeled meteorology from the Weather Research and Forecasting (WRF) model. Predicted Aerosol Optical Depth (AOD) values (annual mean value ~0.2) in CA vary seasonally with lowest values in the winter. Surface $PM_{2.5}$ concentrations (annual mean value ~10 $\mu g/m^3$) also exhibit a seasonal cycle, with peak values and largest variability in the spring/summer, and lowest values and variability in the winter (hourly values from 2 – 90 $\mu g/m^3$). Surface concentrations of black carbon (BC) (mean value ~0.1 $\mu g/m^3$) show peak values in the winter. The simulated values are compared to surface measurements of AOD, and $PM_{2.5}$, PM_{10}, BC, organic carbon (OC) mass concentrations at two regional sites in the Kyrgyz Republic (Lidar Station Teplokluchenka (LST) and Bishkek). The predicted values of AOD and PM mass concentrations and their seasonal cycles are fairly well captured. The carbonaceous aerosols are underpredicted in winter, and analysis suggests that the winter heating emissions are underestimated in the current inventory.

Dust, from sources within and outside CA, is a significant component of the PM mass and drives the seasonal cycles of PM and AOD. On an annual basis, the power and industrial sectors are found to be the most important contributors to the anthropogenic portion of $PM_{2.5}$. Residential combustion and transportation are shown to be the most important sectors for BC. Biomass burning within and outside the region also contributes to elevated PM and BC concentrations. The analysis of the transport pathways and the variations in particulate matter mass and

composition in CA demonstrate that this region is strategically located to characterize regional and intercontinental transport of pollutants. Aerosols at these sites are shown to reflect dust, biomass burning and anthropogenic sources from Europe, South, East and CA, and Russia depending on the time period.

Simulations for a reference 2030 emission scenario based on pollution abatement measures already committed to in current legislation show that $PM_{2.5}$ and BC concentrations in the region increase, with BC growing more than $PM_{2.5}$ on a relative basis. This suggests that both the health impacts and the climate warming associated with these particles may increase over the next decades unless additional control measures are taken. The importance of observations in CA to help characterize the changes that are rapidly taking place in the region are discussed.

1. Introduction

Central Asia (CA), a region of republics located between Europe and Asia, faces severe environmental problems, with origins dating back to the 1960s and best symbolized by the Aral Sea catastrophe (Whish-Wilson, 2002). The Aral Sea has shrunk to only about 30 percent of its 1960 volume and roughly half its geographical size due to diversion of water for crop cultivation and other purposes. The resulting desertification of the lake-bed has resulted in extensive dust storms from the region, which have impacted the surrounding agriculture, ecosystem, and the population's health.

The 2012 Environmental Performance Index (EPI), which tracks performance of 132 countries across a variety of environmental and ecosystem vitality indicators, ranked CA countries among the weakest performers (Kazakhstan 129, Uzbekistan 130, Turkmenistan 131, Tajikistan 121, and Kyrgyzstan 101) (Emerson et al., 2012). CA and the surrounding areas are developing quickly and air pollution emissions are projected to increase significantly for the next several decades (Shindell et al., 2012). In recognition of the need to improve the environmental conditions in the region five CA countries have formulated the Framework Convention on Preservation of Environment for Sustainable Development of CA (UNEP, 2006).

Despite the awareness of the environmental conditions, it remains an understudied region and there is a general lack of air pollution observations within CA. Furthermore the recent assessment of the intercontinental transport of pollution (HTAP, 2010) has indicated that the major transport pathway of pollution from Europe to Asia is via low altitude flows passing through CA. The magnitude of the pollution transport from Europe to Asia is highly uncertain in large part due to the lack of observations of pollutants along this pathway. To help better characterize the air pollution levels and the transport pathways in the region a study was

undertaken between Russia, Kyrgyz Republic, and USA scientists to observe and model aerosols in the region. Measurements of particulate matter (PM) mass and composition were taken at two locations in the Kyrgyz Republic (Lidar Station Teplokluchenka (LST) and Bishkek) and modeling analysis was performed to assess the contributions of local, regional and distant sources to the PM concentrations in the region (Miller-Schulze et al., 2012, Chen et al., 2012, 2013).

In this paper we present a modeling analysis of $PM_{2.5}$, PM_{10}, ($PM_{2.5}$ refers to particles in the size range of less than 2.5 μm aerodynamic diameter (AD) and PM_{10} refers to particles in the size range of less than 10 μm AD), black carbon (BC) and organic carbon (OC) mass concentrations and aerosol optical depth (AOD) over the time period of April 2008 to July 2009. The Sulfur Transport and dEpostion Model (STEM), a hemispheric chemical transport model (D'Allura et al., 2011), is used to estimate spatial and temporal variations in PM in CA, and to assess the contributions to PM from wind-blown dust, open biomass burning, and anthropogenic sources, and different geographical source regions and source sectors (transportation, power, industry and residential). The simulated values are compared to surface measurements of AOD, $PM_{2.5}$, PM_{10}, BC, OC mass concentrations at the two regional sites in CA. The transport of aerosols into CA is also explored through three dimensional backward trajectory analysis. Transport from CA and their impacts on downwind areas are also analyzed via forward trajectory analysis. Finally we present results of how the PM concentrations may change in the future using emission scenarios for 2030 that reflect possible air quality and climate policies.

2. Data and Methods

2.1. Observations

Surface observations from two sites established in the Kyrgyz Republic to measure PM concentrations and AOD in CA are used in the analysis. The locations of the Bishkek (42°40'46.65"N, 74°41'38.13"E, elevation 1743 above sea level (ASL)) and LST (42°27'49.38"N, 78°31'44.17"E, elevation 1921 m ASL) sites are denoted by circle and triangle markers, respectively, in Fig. 1. Both sampling sites are in mountain ranges with valleys to the north, with mountains that reach elevations greater than 3500 m ASL south of the Bishkek site and 4600 m ASL south of the LST site, and essentially no population to the south. At each site, $PM_{2.5}$ mass was measured continuously with tapered element oscillating microbalance (TEOM) instruments and $PM_{2.5}$, PM_{10}, BC, and OC were obtained using filter-based sampling with samples collected for 24 h every other day. AOD was measured every day at 10:30 am local time (LT) using Microtops-II sun-photometers (SP). A stationary three wavelength aerosol Lidar measured vertical profiles of extinction and depolarization on an event basis at the LST site. The Lidar vertical profiles provide information on vertical distribution of the particles, and were also used to calculate AOD from the Lidar Extinction (LE) profiles and to estimate the height of the planetary boundary layer (PBL) as described in Chen et al., (2013). These observations sites are now part of the UNEP project ABC measurement network (http://www.rrcap.ait.asia/abc/index.cfm). Further details of the study can be found in Miller-Schulze et al., (2011). Observations from these sites were obtained for the period April 2008 to July 2009 (the TEOM measurements were available from April 2008 and filter measurements began from July 1, 2008).

In addition, the model prediction skill in simulating the aerosols is evaluated using the AOD observations from the AErosol RObotic NETwork (AERONET available at http://aeronet.gsfc.nasa.gov/) located within the domain and the time period used in this study along with PM_{10} measurements from the European Monitoring and Evaluation Programme (EMEP available at http://www.nilu.no/projects/ccc/emepdata.html) and the Acid Deposition Monitoring Network in East Asia (EANET available at http://www.eanet.asia/product/index.html) surface site networks. Table S1 lists the sites from the AERONET, EMEP and EANET networks used in this study.

The Moderate Resolution Imaging Spectroradiometer (MODIS) collection 5.1 Level 2 AOD products (~ 10 km horizontal resolution) at 550 nm wavelength from Terra and Aqua satellites were used to compare the observed and simulated AOD. The MODIS Level 2 data were used and included land and ocean AOD retrieved via the dark target algorithm (Remer et al., 2005, Levy et al., 2007), and the Deep Blue AOD over land (Hsu et al., 2004, Hsu et al., 2006), which can retrieve AOD over bright and desert surfaces. This is particularly relevant for the CA region, which contains major dust sources in western China, South Asia, the Middle East, and Africa (Ginoux et al., 2001). The MODIS Level 2 to Level 3 averaging procedure outlined in Hubanks et al., (2008) was employed to interpolate the 10 km Level 2 AOD products to the 60 km horizontal model resolution on a daily basis. Level 2 QA flag weightings were used to reduce the uncertainty associated with the MODIS retrievals. In grid cells where both the MODIS dark target and Deep Blue AOD were retrieved, the mean value of the two was used.

2.2. Modeling System

2.2.1 Meteorological Model

153 The Weather Research and Forecasting (WRF) model (Skamarock et al., 2008) version
154 3.2 was used to generate the meteorological fields needed for simulating the transport patterns in
155 the STEM model (D'Allura et al., 2011). The WRF simulations for each day were initialized
156 using the meteorological boundary conditions obtained from National Centers for Environmental
157 Prediction (NCEP) Final Analysis (FNL, http://rda.ucar.edu/datasets/ds083.2/). A daily 24 hour
158 spin up time for WRF was used (i.e. WRF was run for 48 hours each day and the first 24 hours
159 were treated as spin up and were discarded). The STEM model simulation time period was from
160 April 2008 to July 2009.

161 2.2.2 Chemical Transport Model

162 The STEM model (Carmichael et al., 2009) was used to simulate the mass of sulfate, BC,
163 OC, other primary emitted $PM_{2.5}$, and other primary emitted PM_{10} (i.e., non-carbonaceous PM
164 such as fly ash, road dust, and cement), which were simulated as a single mass component with
165 aerodynamic diameters less than or equal 2.5 μm, and between 2.5 and 10 μm (denoted as coarse
166 fraction), respectively and referred to in this paper as $OPM_{2.5}$ and OPM_{10}, dust (fine and coarse)
167 and sea salt (fine and coarse). Nitrate and secondary organic aerosols (SOA) were not included in
168 the model for this application. The nitrate aerosol is estimated to be a minor component of the
169 PM mass in CA (Baurer et al., 2007). The importance of SOA will be discussed later in the
170 paper. The dry deposition of aerosols was modeled using the "Resistance in Series
171 Parameterization" (Wesely and Hicks, 2000) and wet deposition was calculated as a loss rate
172 based on the hourly precipitation calculated from the WRF model. Further details of the wet
173 scavenging can be found in Adhikary et al., (2007). The modeled AOD at 550 nm wavelength

was calculated using the simulated three dimensional aerosol distributions and species specific extinction coefficients as described in Chung et al., (2010).

2.2.3 Modeling Domain

The STEM and WRF computation domains were identical, with a 60 ×60 km horizontal resolution (249 ×249 horizontal grid cells) and 22 vertical layers up to 10 hPa. The domain (Fig. 1) covered much of the northern hemisphere in a polar stereographic projection, centered over the Arctic region and extended to 35° N to include the major emission regions of North America, Europe, and Asia. This modeling system has been applied to simulate aerosol distributions for ARCTAS field campaign as described in D'Allura et al., (2011) and further details describing the model can be found there. STEM was initialized with a one month spin up using March 2008. Much of the analysis for this paper is focused on the domain denoted by the rectangle centered over CA shown in Fig. 1. This domain has large gradients in topography (insert Fig. 1), which significantly impact the transport patterns in the region.

2.2.4 Air Mass Trajectories

The CA observation sites are impacted by dust, anthropogenic pollution, and biomass burning emissions from various source regions. To further understand the transport pathways and source region influences on the PM distributions at these sites, three dimensional ten day air mass trajectories (both forward and backward in time) from each site were calculated for the entire time period (April 2008 – July 2009). In this trajectory analysis, we utilized the three dimensional wind fields (including u, v and w components) along with the above ground level

(AGL) altitude simulated by the WRF meteorological model consistent with Dallura et al., 2011 study. These trajectories describe the general flow patterns based on wind fields alone and provide useful information about the history of air mass particularly the influence of source regions over which the air mass had resided before arriving at the site of interest. Note that these trajectories do not account for any other atmospheric processes such as diffusion or chemical evolution along its path (Kurata et al, 2004 and Guttikunda et al., 2005).

To understand the differences in transport patterns at the surface and aloft, and to study the impact of topographic gradients in the vicinity of the sites, trajectories were initialized at different altitudes (0.1 (100m), 0.3 (300m) 0.5 (500m), 1, 2, 3, and 5 km) a.g.l at the site locations (i.e. latitude and longitude) daily every 3 hours for a ten day period both backward and forward in time. The trajectories were terminated when they touched the ground, or went out of the model domain or exceeded the ten day calculation period. The trajectories (at or below 1 km) were used to characterize transport pathways impacting the surface concentrations at these sites, which are discussed later in section 3.5.

2.3. Emissions

2.3.1 Base emissions

Anthropogenic emissions of BC, OC, $PM_{2.5}$, PM_{10}, and SO_2 were based on the ARCTAS emissions described in D'Allura et al., (2011), but updated with newly available information. For India and China BC, OC, and SO_2 emissions from Lu et al., (2011) were utilized, and INTEX-B emissions were used for the rest of Asia (Zhang et al., 2009). For Europe, the EMEP 2008 (http://www.ceip.at/webdab-emission-database/officially-reported-emission-data) emissions were used for SO_2, $PM_{2.5}$, and PM_{10}, and the EUCAARI 2005 inventory was used for the

221 carbonaceous particles (BC and OC) (Visschedijk et al. 2009 and Denier van der Gon et al.
222 2009). The shipping emissions came from the IIASA base year 2005 inventory (UNEP and
223 WMO, 2011). Mass conservative regrinding tools including MTXCALC and MTXCPLE from
224 the IOAPI m3tools suite (http://www.baronams.com/products/ioapi/AA.html#tools) were used to
225 interpolate the input raw emissions described above on to the model grid.

226 Anthropogenic emissions for SO_2, BC and OC were available by major economic sectors;
227 i.e., transportation, residential, industry, and power. The industry and power sectors were treated
228 as small and large point sources, respectively, and emitted into the first 6 model levels (lowest 2
229 km). The residential and transportation emissions were treated as near surface area sources and
230 partitioned into the first two model levels from surface to ~ 100m (i.e. AGL altitude of level 2)
231 with a 90 – 10 percent split. Monthly emission allocation factors were applied over India and
232 China for the economic sectors from Lu et al., (2011). The rest of the domain (i.e. excluding
233 India and China) used same emission rates for all months due to unavailability of monthly
234 emission allocation factors.

235 The Fire Inventory from NCAR (FINN v1) was used for BC, OC, CO, SO_2, $PM_{2.5}$ and
236 PM_{10} biomass burning emissions from forest, grassland and crop residual fires. The FINN
237 database, which is based on MODIS fire detection as thermal anomalies, provides global
238 coverage of fire emissions at a spatial resolution of ~ 1km on a daily timescale (Wiedinmyer et
239 al., 2011). The WRF-Chem fire utility (http://bai.acd.ucar.edu/Data/fire/) was employed to
240 interpolate the speciated FINN emissions to the WRF model grid. The gridded two-dimensional
241 FINN emissions were used as input to the WRF-Chem (Grell et al., 2005) plume rise model
242 (Grell et al., 2011), which implements the Freitas et al., (2007) and Freitas et al., (2010)

algorithm to compute injection heights and to calculate the vertical distribution of fire emissions at an hourly time step, which were further utilized as input to STEM model simulations.

Sea salt and dust emissions were calculated using the WRF meteorological fields based on the methods described in Gong, (2003) and Uno et al., (2004), respectively. The dust emissions were further constrained with snow cover (SNOWC variable from WRF output) and only grid cells with snow cover < 1% were used for dust emission calculations.

Fig. 2 shows the annual gridded anthropogenic SO_2 and BC, dust, and biomass burning $PM_{2.5}$ emissions in Gg per grid in and around CA. Large BC emission hotspots can be seen over the Indo-Gangetic plain and eastern China. Significant BC emissions are also seen over Europe, but are relatively lower in intensity than the Asian sources. The SO_2 emissions show Eastern China as the largest source region followed by regions of South Asia, Europe, and Russia. The major natural dust emission sources (Fig. 2c) include Africa, the Middle East, CA, Western India boundaries, and Western China. The major sources of biomass burning are Eastern Europe, portions of Siberian (between 40 – 60° N), Southeast Asia, Southern China and India (Fig. 2d).

Dust emissions have a strong seasonal cycle. The major dust sources in the region (Fig. 1) are located to the east, west and south of the observation sites and include the cool winter deserts around the Aral and Caspian seas and those in western China and northern Pakistan as well as the sub-tropical deserts in western India, around the Persian Gulf and northern Africa. The emissions from the cool winter deserts occur when the surfaces are free of snow cover (from March through October). Emissions from the sub-tropical deserts can occur throughout the year.

263 The open biomass burning emissions that impact CA also have a strong seasonality with
264 minimum impact in winter (Supplemental Materials Fig. S1). Fires typically begin in the spring
265 in Siberia along 50° N latitude and in northern India and South East Asia and in summer the high
266 latitude burning shifts to the west. In October the fire activity decreases and remains low until
267 spring, with the most active fire regions associated with agricultural burning in northern India
268 and southeast China.

269 **2.3.2 Future Emissions Scenarios**

270 In addition to the base emissions, a series of simulations were analyzed using emission
271 scenarios for 2030. These scenarios were developed for the WMO/UNEP report that looked at
272 short lived climate pollutants as described in Shindell et al., (2012) and Anenberg et al., (2012).
273 The reference scenario for 2030 was based on the implementation of control measures currently
274 approved in the various regions and assumed their perfect implementation. The 2030 reference
275 scenarios were developed from a reference global emissions inventory with a 2005 reference
276 year, and assumed significant growth in fossil fuel use relative to 2005, leading to increases in
277 estimated CO_2 emissions (45%). Abatement measures prescribed in current legislation were
278 projected to lead to reductions in air pollutant emissions, which varied by pollutant and region.
279 In the 2030 reference scenario, total primary $PM_{2.5}$ emissions remain approximately constant,
280 while BC and OC decline by a few percent. However, in the study domain emission changes
281 varied widely. BC emissions increased by 10 – 100% in CA, South and Southeast Asia and in
282 western China, and decreased in East Asia and Europe. The $PM_{2.5}$ emissions showed similar
283 regional changes but grew at smaller rates (10 – 40%). SO_2 emissions generally increased

284 throughout the region by 10 – 20%. Spatial maps of emission changes for the 2030 reference
285 scenario are presented in Figs. S2b, S3b, and S4b.

286 A series of emission control scenarios for 2030 were developed to evaluate the impact of
287 additional abatement measures designed to reduce the levels of short lived climate pollutants
288 (e.g., BC). The BC measures in the scenarios included two different sets of assumptions (low and
289 lowest). The first focused on reductions from incomplete combustion sources. These included
290 implementation of Euro 6 equivalent vehicle emission standards (requiring installation of diesel
291 particulate filters) and improving traditional biomass cook stoves in developing countries
292 (assuming 25% decrease in BC and 80 – 90% decreases in OC, CO, non-methane volatile
293 organic compounds(NMVOC), methane, and direct $PM_{2.5}$, relative to emissions from traditional
294 stoves). Under this scenario BC and $PM_{2.5}$ emissions in the study region are projected to decrease
295 throughout most of the domain, with SO_2 emissions showing almost no change (see Figs. S2c,
296 S3c, and S4c).

297 The lowest option assumed the additional elimination of high-emitting vehicles, biomass
298 cook stoves (in developing countries), and agricultural waste burning. These BC measures in the
299 lowest scenario reduced global anthropogenic BC emissions by 75%. Measures targeting BC
300 also substantially reduced total primary $PM_{2.5}$ (-50%), OC (-79%), NO_x (-27%), and CO (-44%).
301 These BC measures have little impact on SO_2 emissions. Projected emissions of BC and OC
302 under these scenarios are reduced most in Asia, followed by Africa. North America, and Europe.

303 These measures were also combined with a scenario designed to stabilize greenhouse
304 gases at 450 ppm of CO_2 equivalent (lowest+450ppm scenario), consistent with a global average
305 temperature increase of ~2° C. These CO_2 measures reduced SO_2 (-30%) (Fig. S4d) and NO_x (-

306 20%), but had little further impact on BC (~5% decline, Fig. S2d) since the major sources of CO_2
307 differ from those of BC. $PM_{2.5}$ emissions were substantially further reduced under this scenario
308 (Fig. S3d).

309 **2.4. Simulations Analyzed**

310 The CA region is strategically located and aerosols at these sites are shown to reflect
311 impact of varied dust (including CA, Western China, Africa and Middle East), biomass burning
312 (including Europe, Siberia, South Asia and North America) and anthropogenic sources
313 (including Europe, South, East and Central Asia, and Russia) depending on the time period. So
314 we choose different regions for the anthropogenic, dust and biomass burning in order to capture
315 the impact and the associated seasonality of these main regions on the regional distribution of
316 aerosols in this region. We have more anthropogenic regions to better understand how regional
317 changes in emissions may impact CA PM levels.

318 Several simulations were analyzed for this paper. The *base* simulation included all
319 sources and used the meteorology from the WRF model for the period April 2008 – July 2009.
320 To investigate the contributions from specific source sectors, additional simulations were
321 performed where emissions from one sector were set to zero everywhere. The contribution from
322 each sector was calculated as the difference between the base simulation and the simulation with
323 emissions from that particular sector set to zero. This was repeated for each sector and for
324 biomass burning. Additional simulations were performed to assess the source contribution from
325 specific regions to the particle levels in CA. The specific regions used are shown in Fig.1. In
326 these simulations all anthropogenic emissions were set to zero in that region. In a similar manner
327 regional dust and fire sources were also studied and the source regions are also shown in Fig.1.

328 Finally, simulations were performed using the *reference* 2005 and 2030 emissions and the *low*
329 and *lowest + 450 CO_2* 2030 scenarios (described above). For these runs, the meteorology, open
330 biomass burning, and dust emissions were the same as in the base run (i.e., 2008/2009).

331 **2.5. Model Evaluation**

332 We have evaluated this model framework in other regions outside CA including arctic region and
333 continental US previously, which are summarized below. The domain configuration and settings
334 of the WRF/STEM modeling system used in this study have been applied to provide
335 meteorology and air quality forecasting during the ARCTAS field campaign in 2008 (Dallura et.
336 al., 2011) as mentioned earlier in sections 2.2.3 and 2.3.1 respectively. The study by Dallura et
337 al., used WRF v2.2 and pre-emission ARCTAS emissions data
338 (http://mic.greenresource.cn/arctas_premission), real time biomass burning emissions from the
339 RAQMS modeling group (http://raqms-ops.ssec.wisc.edu/) and evaluated the performance of the
340 WRF-STEM modeling framework (used in this study) through the case study of the ARCTAS
341 mission DC-8 flight conducted on July 9 2008. The WRF model compared well with observed
342 meteorological variables (including temperature, pressure, wind speed and wind direction) along
343 the flight and correctly simulated the various meteorological processes (i.e. cyclonic circulation,
344 low pressure system, anticyclones and geostrophic wind flows) that facilitate transport of
345 pollutants into the Arctic region. This study also compared CO along the flight and found that
346 the simulated values were able to capture the magnitude and temporal variability seen in
347 observed values. The study also found that the fires from North Asia and anthropogenic CO from
348 China were the major sources contributing to observed CO levels along the flight suggesting that

349 the midlatitude pollution and summertime forest fires/biomass burning transport events were
350 well represented in this modeling system.

351 Huang et al, 2012 used a subset of this domain (covering the region of continental North
352 America) to simulate summertime sectoral and regional contributions to BC over continental US
353 using the WRF/STEM modeling framework. Note that the Huang et al., 2012 study used the
354 same WRF meteorology, ARCTAS emissions and RAQMS biomass burning emissions used in
355 the Dallura et al., 2011 study, but used the full-chemistry version of the STEM model. The
356 comparison of the simulated aerosol BC from the STEM tracer model with corresponding BC
357 values from the full chemistry version of the STEM model showed that the simulated tracer BC
358 was able to capture trend and the same relative variability seen in the full chemistry predictions.
359 Huang et al., 2012 evaluated the model performance aloft and at surface using measurements
360 from ARCTAS mission DC8 flights conducted on June 20 and 22 and 24 that sampled over
361 California and IMPROVE surface site network. Huang et al., 2012 found that the predicted BC
362 values captured many of the vertical features seen in the flight observations with a tendency to
363 over predict surface BC and > 4km. The comparison of predicted BC with observed values from
364 the IMPROVE network showed that the model was able to capture the gradients in BC values
365 with high concentrations in western and eastern NA regions with slight positive and negative
366 biases over the mountain regions and the eastern US/California. In this paper we further evaluate
367 the performance of the model over the selected domain in this study (Fig. 1) using MODIS and
368 AERONET AOD and PM_{10} surface observations as described in the following sections.
369

370 **3. Results and Discussion**

3.1 Regional Perspective

CA is a region with high aerosol loadings as shown in the mean MODIS retrieved AOD at 550 nm for the time period of study (April 2008 – July 2009) (Fig. 3a). AOD (period mean) throughout CA (~ 45-90° E, 35-50° N) are greater than 0.25, with the highest regional values around the desert areas near the Caspian and the Aral seas. There are also high values (>0.6) along CA's eastern border, which reflect the deserts and rapidly developing cities in western China, and to the south over Pakistan and northern India.

The period-mean predicted surface concentrations of $PM_{2.5}$, BC, total dust (fine and coarse) and $PM_{2.5}/PM_{10}$ ratio are shown in figure 4. The BC levels in CA are typically less than 0.3 $\mu g/m^3$ and its spatial pattern reflects contributions from both anthropogenic and biomass burning sources (Fig. 4a). The simulation period mean $PM_{2.5}$ concentrations in CA (10 to 35$\mu g/m^3$) (Fig. 4c) have a similar geographical distribution as AOD (Fig.3a). Dust is the major component of predicted PM_{10} in CA as seen from the high dust concentrations (25-100 $\mu g/m^3$) in Fig. 4b and low values (0.3 – 0.4) of the predicted $PM_{2.5}/PM_{10}$ ratio (Fig. 4d). The natural dust source regions including Western China, Middle East, Africa and western India have similar $PM_{2.5}/PM_{10}$ ratio values (0.3-0.4) reflecting the major contribution of dust to PM over these regions. The high predicted $PM_{2.5}/PM_{10}$ ratio values (>0.6) are seen over southern and eastern China indicate that the non-dust sources are the dominant contributors to PM in this region.

3.2. Model Evaluation with AOD and PM measurements

3.2.1 Comparison with MODIS and AERONET AOD

393 The predicted period mean AOD spatial distribution is shown in Fig. 3b (using only data
394 from grid cells where MODIS AOD was available. The white colored areas denote regions
395 where MODIS AOD data was not available). The simulated AOD values capture the main
396 observed spatial features including enhanced AOD over desert regions of Asia including East
397 Asia, West Asia and along the western border of India, Eastern China, Northern India covering
398 the Indo Gangetic Plain and Southeast Asia that are known to have large impacts of
399 anthropogenic and wildfire emissions. However, the period mean AOD values are biased low
400 relative to MODIS AOD over the regions of Northern India and Eastern China. This could be in
401 part related to uncertainty associated with anthropogenic emissions over these regions and the
402 60km model resolution used in this study. The simulated AOD values are overpredicted relative
403 to MODIS AOD over regions surrounding CA including parts of Eastern Europe, Russia,
404 Northern China, Western Asia and Africa. These biases could be partly attributed to the
405 uncertainty associated with regional transport of dust shown in spatial patterns of simulated dust
406 and $PM_{2.5}/PM_{10}$ ratio (Fig. 4b and d).

407 The model prediction skills in simulating the temporal and spatial patterns in AOD was
408 evaluated by comparing the predicted daily AOD with the corresponding measured values at 142
409 sites from the AERONET program (See Table S1 for AERONET site details) located within the
410 domain and for the time period used in this study. We have also compared the AERONET AOD
411 with MODIS on a daily time scale by extracting the daily MODIS retrieved AOD corresponding
412 to the AERONET site locations for the simulation time period. The comparison of the predicted
413 daily AOD with the available MODIS retrievals (n = 29680 using MODIS and simulated AOD
414 extracted at the AERONET site locations, which are paired in space and time) is shown in Fig
415 3c. The model values show a similar mean value (average simulated and MODIS AOD are 0.24

and 0.31 respectively), with a negative bias and an underprediction in the variability. The comparison of model predictions with respect to AERONET AOD data (n = 22875) shows much closer agreement with mean modeled and AERONET values of 0.21 and 0.23 respectively; (note the comparison is based on paired data for the times only when AERONET data was available so the means are different than the MODIS/model comparison). Also shown is the comparison between MODIS and AERONET (for times/locations with paired AERONET measurements; n = 12719) with AERONET and MODIS mean values of 0.24 and 0.29 respectively. The comparison results of AERONET with respect to MODIS are similar to corresponding values of the MODIS/MODEL comparison, indicating that MODIS retrievals are biased high in the study domain. A more detailed analysis of the AOD comparison by region and season is included in the Supplemental Materials (Table S2 and Figs. S5 and S6)..

3.2.2 Comparison with PM_{10} observations from EMEP and EANET network

We also evaluated the simulated PM_{10} values with monthly mean observed data for the simulation time period from the EANET network over Asia (see Fig. S7). The modeled values are underpredicted as evident from the mean observed and modeled PM_{10} values of 32.2 and 22 $\mu g\ m^{-3}$ (n = 314). The normalized mean bias and error are ~ -32% and 44 % respectively. This could be partly attributed to the uncertainty associated with dust emissions that have a significant impact on the EANET site locations (See Table S1 for PM_{10} site locations). We also evaluated the simulated PM_{10} values over Europe using the available monthly mean observations from EMEP for the 2002-2003 time period (See Table S1 for EMEP PM_{10} site locations). The mean observed and modeled values of PM_{10} are 23.9 and 22.2 $\mu g\ m^{-3}$ (n = 130). The normalized mean

bias and error for the EMEP PM_{10} are -7 and 43 % respectively suggesting an overall underprediction by the model.

The evaluation of this model framework in other regions outside CA including arctic region and continental US (described earlier in Sect. 2.5) along with the comparison of regional distribution and temporal variability in simulated AOD using corresponding MODIS and AERONET measurements indicates that the predictions of aerosol mass and composition at the hemispheric scales are able to capture important aspects of horizontal gradients and variability, but have considerably higher uncertainties associated with emission estimates (in particular forest fires/biomass burning and natural dust emissions) and wet removal processes (Bates et al., 2006).

3.3 Comparison with surface observations in CA

The surface observations at the two CA sites provide the opportunity for the first time to evaluate the performance of chemical transport models in estimating the distribution of aerosols in CA and to assess the emission estimates in the region. A comparison of the predicted and observed meteorology is presented in Fig. 5, where the distributions of key meteorological parameters for the entire measurement period are shown as box-plots. The model accurately predicted the magnitude and variability in temperature and relative humidity. For example the model mean value of temperature and relative humidity are 279.3K and 61.6% in comparison to the observed values of 280.3K and 59.2% at the LST site. The model wind speeds were biased high by about 30% (mostly in winter, see section 3.4) and the direction had a southwest bias. These biases are due in part to the 60 km model grid size, which is too coarse to capture the steep gradients in topography in and around the observation sites, and to the site placement in small N-

S oriented valleys. More details regarding the evaluation of the modeled meteorology can be found in the Supplemental Materials, Table S3.

The observed and modeled distributions of AOD and PM are compared in Fig. 6. The AOD observations based on the LE on average are ~50% larger than those from the SP. Modeled AOD on average are ~20-30% higher when compared to SP at the Bishkek and LST sites and ~1 % lower when compared to the LE values. The variability in the predictions is slightly under-estimated. $PM_{2.5}$ is over predicted (~50%) and the spread is accurately captured, while PM_{10} is over predicted by ~70%. This leads to an underestimation of the $PM_{2.5}/PM_{10}$ (0.4 predicted versus 0.5 observed) and also helps account for the overestimation in modeled AOD (by ~20-30%).

Chemical analysis of the filter and soil samples in the CA dust regions have been used to estimate the dust contribution to measured PM at the two sites and to help identify source regions of importance (Park et al., 2014). The emission regions within CA, including around the Aral Sea, and western China were identified as the most important dust sources, which is consistent with the regions identified in the simulations. Dust was estimated to comprise between 5-40% of $PM_{2.5}$ mass at the LST site and to vary by season (minimum values in winter). The observation-based estimates of dust percentage contribution suggest that modeled dust is over predicted by ~2 times. Thus it appears that dust is a main reason for the over prediction of $PM_{2.5}$ and PM_{10}, and that dust emission models need to be refined for CA applications.

The overestimation in PM mass at the surface could also be impacted by errors in the modeled PBL heights. The PBL height as determined by the Lidar aerosol profiles varies seasonally and is highest in the summer (from 2-4 km AGL) and lowest in the winter (Nov-Feb,

0.5-1.5 km AGL) (Fig. S5). The predicted PBL heights show a similar seasonal cycle with a tendency to under-predict the heights in all seasons as indicated by the comparison of the distributions of the observed and predicted values (Fig. 5), and this occurs in all seasons (Fig S8). The lower PBL height in the model contributes a systematic high bias in surface concentrations driven by near surface emissions. Further statistical details of the model-observation comparison can be found in the supplemental materials (Table S4). The seasonal variability in the observations is discussed in further detail later (section 3.4).

3.4 Source Contributions to $PM_{2.5}$

Model simulations were performed to identify the component, source region and emission sector contributions to $PM_{2.5}$ mass. Period means for the spatial average over the entire CA region (see Fig. 1) and for the grid cells for the Bishkek and LST observation locations are presented in Fig.7, and their comparison provides insights into the spatial variability of PM and its sources within CA, and how representative the observation sites are at characterizing CA PM. The component contribution to AOD at the sites and for the CA average are similar, with the major contributions coming from fine dust, sulfate, and OC. Spatial maps of mean percent contributions of the various components (i.e., BC, OC, sulfate, OPM, dust and sea salt) to AOD and $PM_{2.5}$ mass are presented in Figs. S9 & S10, respectively. Coarse particles contribute ~10% to mean AOD. Dust accounts for >60% of the calculated $PM_{2.5}$ mass at the observation sites and for the CA region. The dust source regions (see Fig. 1) contributing to $PM_{2.5}$ vary within CA. Dust from the CA source regions has the largest influence on the region mean dust- $PM_{2.5}$ mass. At the LST site, which is located in the far east of CA, western China dust sources have their largest influence (~40%). African and Middle East source regions have their largest influence on

503 the Bishkek site (20 and 15%, respectively), and collectively contribute ~25% to regional CA
504 dust $PM_{2.5}$.

505 The source region contributions to the non-dust $PM_{2.5}$ are very similar for the Bishkek
506 and LST sites, with CA sources making the largest contribution (~50%) followed by Europe
507 (~20%), the Middle East (~15%), and biomass burning (~15% from all sources). For the entire
508 CA region the European source contribution is as large as the CA sources (~30% each), with
509 larger contributions from biomass burning and Russia sources and smaller contributions from
510 Middle East emissions than at the observation sites. The significant contribution from Europe
511 sources reflects their large anthropogenic emissions and the general westerly transport patterns.
512 On average the impact from South Asia sources are small. North America sources contribute
513 between 3 to 7% to $PM_{2.5}$ in CA. Of the biomass burning contribution to $PM_{2.5}$, the Siberian and
514 European fires (see Fig. 1 for fire regions) contribute 63 and 25%, respectively, with
515 contributions from South/Southeast Asia and North America fires each contributing ~5%. The
516 power and industrial sectors are identified by the simulations as the largest contributors (~40%
517 each) to non-dust $PM_{2.5}$ mass in CA.

518

519 **3.5. Seasonal Variations in AOD and PM at the Observation Sites**

520 AOD has a seasonal cycle with the lowest values in winter and highest values in spring
521 and summer as shown in Fig. 8 by the AOD observations at the LST site from both the SP and
522 the LE profiles. A similar seasonal cycle was observed at the Bishkek site (not shown) and in

523 the MODIS AOD retrievals (Fig. S11). The modeled AOD captures this seasonal variation, with
524 a tendency to over predict the values during the periods with the lowest observed AOD.

525 The seasonal cycles in $PM_{2.5}$ (Fig. 9) and PM_{10} are similar to those for AOD, with
526 minimum values in October – February. At the LST site $PM_{2.5}$ from both the filter based and the
527 non-volatile TEOM measurements are plotted. Both the observations and the model find a strong
528 similarity in the time series at the two sites.

529 There is also a clear seasonality in the surface meteorology in the region as shown by the
530 time series in surface temperature and relative humidity at the two sites (Fig. 10). There are
531 distinct temperature minima in the winter and relative humidity minima in the summer. However
532 there is not a clear seasonality in wind speed and direction, and the winds are generally from the
533 south and less than 4m/s throughout the year at the LST site (not shown).

534 The source region and component contributions exhibit seasonal variability as shown by
535 the modeled contributions to $PM_{2.5}$ mass in Fig. 11. Dust is found to be the main driver of the
536 seasonal cycle of $PM_{2.5}$. The dust contribution to $PM_{2.5}$ is peak in spring and minimum in winter
537 (<20%). During this time period the transport of air masses to the sites are from the west and the
538 southwest. When the transport is from the east then dust sources from western China can impact
539 the stations. This transport pattern occurs episodically throughout the year, with contributions
540 from western China sources as large as 20 to 50%. The dust seasonal cycle is in turn influenced
541 by the seasonal variations in meteorology that drives the dust emissions and transport. The
542 seasonal changes in the dust source regions can be seen in the seasonal spatial maps of AOD
543 (Fig. S11). Throughout the domain, AOD in the dust regions are highest in March – October and
544 lowest in winter (Fig. S11) as the nearby desert regions are snow covered.

Biomass burning also adds to the seasonal cycle, and its contribution is minimum in the winter. South Asia sources can impact the sites in the winter time. The periods when North America sources impact the site are associated with strong transport events across the Atlantic and subsequent subsidence towards the surface associated with high pressure systems as they move towards CA. The transport pathways are discussed in more detail in Sect. 3.7.

3.6 Source Contributions to BC

Because of its dual role as an air pollutant and as a climate warming agent there is special interest in understanding the regional and sector contributions to BC (Ramanathan and Carmichael, et al., 2008). BC comprises on average only about 1-2% of $PM_{2.5}$ mass in CA. The period mean predicted BC surface concentrations are ~0.1 $\mu g/m^3$ at the two observation sites and 0.15 $\mu g/m^3$ for the CA regional average. As shown in Fig. 7, European emissions contribute ~50% to the mean BC concentrations in CA, while Middle-eastern and biomass burning sources each contribute ~15-20%. Residential and transport are the most important sectors each contributing ~30% to BC in CA, followed by industry (~20%), and with power the least important. This is in contrast to the sector contributions to non-dust $PM_{2.5}$ mass, where power and industry are the most important sectors. On average biomass burning contributes ~10% to BC mass, with Siberian and European fires accounting for 61% and 33%, respectively. The source contributions to OC are shown in Fig. S12.

There is also large seasonal variability in BC concentrations and source sector/region contributions (Fig. 12). BC surface concentrations show the highest values in fall/winter (as do the observations), when there is maximum contribution from the residential sector, reflecting the wide-spread use of biofuels and coal for heating in the region. The source region contributions

567 vary by season, with maximum contributions from Europe and China. South Asia sources
568 contribute in the winter. Biomass burning also is an important source of BC and plays an
569 important role in influencing daily and seasonal variability in BC concentrations.

570 Predicted BC captures the seasonality and the magnitude of the spring and summer
571 values as observed, but concentrations are biased low in the fall/winter. Median BC
572 concentrations (and variability) are underestimated by a factor of 2 at both observation sites (Fig.
573 6 and Table S4)). The high wind speed bias in winter (~ factor of 2), should result in too rapid
574 dispersion and could contribute to the negative bias, but the negative bias in the PBL heights
575 should lead to higher predicted concentrations. Thus this negative bias is likely related to
576 emissions (an indication of an underestimation of the heating fuel use).

577 The OC concentrations follow a similar seasonal cycle as BC and are also under
578 predicted (Fig. 6 and Table S4)). Furthermore the OC/BC ratio is under predicted by a factor of
579 ~3 (Fig. 6). The observed OC/BC ratio follows a seasonal cycle with values >15 in summer and
580 ~5 in September through April. Part of this under prediction in OC and the OC/BC ratio is due to
581 the fact that SOA is not estimated in the model. However a source contribution of OC using the
582 filter data and chemical mass balance (CMB) approach found that SOA sources were very low in
583 winter and only ~ 20% in summer (Miller-Schulze et al., 2011). Thus SOA cannot account for
584 the model under prediction of winter values. There appears to be an underestimation of regional
585 OC primary emissions. SOA can however help account for the large values of OC/BC observed
586 in the summer and not predicted.

587 Biomass burning emissions cannot account for the underestimation in winter BC and
588 OC. The largest impact of fires at the observation sites is in the late summer, when the fires are

589 concentrated in western Russia and the wind direction is such that the smoke is transported into
590 CA. Fires from South Asia can impact the sites associated with the fires and high pollution levels
591 in northern India and with winds from the south, which can occur in late fall, but not frequently.

592 The fact that BC and OC are systematically under predicted in the winter suggests that
593 local/regional emissions during the heating season may be underestimated. This is supported by
594 the results of the CMB analysis of OC discussed above that found the contribution from biofuel
595 combustion increased 2-3 times in the fall and winter periods. The uncertainty in emissions can
596 also be partly caused by the lack of seasonal emissions over this region as described earlier in
597 section 2.

598

599 **3.7 Vertical Distributions**

600 Figure 13 shows the predicted weekly averaged vertical distributions of $PM_{2.5}$, dust, and
601 BC for the entire simulation period at the LST site. These plots show more clearly that much of
602 the variability in the PM loadings is associated with dust and biomass burning episodes (as
603 represented by the enhancements in BC). Typically the high PM episodes show elevated PM
604 mass that extend from the surface to 2 to 4 km. The vertical extents show a seasonality
605 associated with seasonal variations in the PBL heights. These vertical distributions indicate that
606 much of the transport of aerosols in CA occurs via low altitude pathways. In some cases there are
607 large amounts of dust and biomass burning aerosol in the 3-6 km altitude range that are
608 decoupled from the surface (e.g., dust in early May 2009), reflecting that some aerosols are lifted
609 out of the boundary layer and are transported at high altitude over CA, enhancing AOD but not

610 contributing to ground-level mass concentrations at the observation sites. These vertical features
611 are confirmed by the aerosol extinction profiles observed at the LST site as discussed in Chen et
612 al., (2012 b). The variation in weekly averaged AOD can be significant (Fig. 13 bottom panel)
613 and is driven by variations in dust and biomass burning emissions.

614

615 **3.8 Transport Pathways**

616 The three dimensional ten day air mass trajectories (described in section 2.2) were utilized to
617 further understand the transport pathways of air masses entering into and exiting out of the CA
618 region and its subsequent impact of source regions on the aerosol distributions at the CA sites.

619

620 3.7.1 Transport into CA

621 The air mass transport into CA is discussed through back trajectories associated with the
622 five events labeled on Fig. 13. These five events represent transport episodes with elevated
623 surface $PM_{2.5}$ (averaged over the three hour time window consistent with trajectory time step)
624 with varying contributions from biomass burning, anthropogenic pollution, and dust sources. In
625 each trajectory figure (Figs. 14 and 15), the regions with active dust (blue diamond hatches) and
626 biomass burning emissions (green square hatches) for the event time period and prior ten days
627 are identified and MODIS AOD (values printed in black) overlaid. The trajectories are color
628 coded by region to distinguish the source impacts. The regions include: Africa (blue), Middle
629 East (green), CA (yellow), North Asia biomass (> 50° N, black), Europe (brown), China (red)
630 and South Asia (orange).

631 Figure 14 shows the first two events for August 2008. The first event in early August
632 (Fig. 13, event labeled 1) is a high dust event associated with trajectories from the west passing
633 over the dust regions of the Aral Sea (~45N, 55E) and eastern trajectories passing over the
634 Taklimakan region of western China (90-100E, 40N). These were both regions with active dust
635 emissions as indicated by the elevated MODIS AOD values. Thus the PM increases during this
636 event were due largely to dust emitted from CA and western China deserts. The second event in
637 the latter half of August is characterized by high levels of BC without dust. During this episode
638 the transport to the site was under the influence of a high pressure system located to the
639 northwest and air masses were transported over the active fire region in western Russia.

640 Figure 15 shows winter and spring events. The November episode (event 3) is a period
641 with elevated BC and $PM_{2.5}$ from pollution sources from South Asia (including some fires) and
642 western China and low fire and dust emission activity. The January episode (event 4) is a period
643 of elevated BC with air masses coming from Europe, indicating the influence of anthropogenic
644 pollution coming from this industrialized region, and from CA sources. Dust emissions from CA
645 and Africa were low during this period. The final illustrative episode is for April 2009 (event 5),
646 a period with both elevated levels of dust from western China, CA and Africa and BC from both
647 fire and anthropogenic pollution from Europe, CA and Russia sources.

648 These examples provide insights into the source region contributions to PM mass in CA
649 as presented in Figs. 11 & 12). CA is an ideal location to observe a variety of source regions as it
650 is at the crossroad of transport patterns with air masses impacted from dust, anthropogenic
651 activity and biomass burning from different geographical regions.

652 3.7.2 Long range transport of CA sources

653 The transport pathways out of CA were also evaluated by calculating forward trajectories
654 from the observation sites. Selected forward trajectories initialized at or below 1 km are used to
655 represent the transport of boundary layer PM from CA and these are shown for summer, winter
656 and spring periods in Fig. 16. In these plots the MODIS AOD, dust, and fire emissions plotted
657 for each event represent values averaged over the subsequent ten days and trajectories were
658 stopped if they impacted the surface. During the summer, outflow from CA is towards the north
659 in association with the summer monsoon system. Figure 16a shows the subset of forward
660 trajectories that reside for at least 3 days over the region 48 - 65° N during June 2008.
661 Trajectories typically pass over Russia and reach into the Arctic and also can be caught in
662 westerly storm tracks and reach the higher latitudes of the northern hemisphere. During the
663 winter, air mass transport out of CA is associated with the winter monsoon system and the
664 transport pathway is over Mongolia and then over eastern China as seen in Fig. 16b. In this
665 figure, forward trajectories that pass over the region west of 130° E during late December 2008
666 are shown. Figure 16c illustrates transpacific transport of CA air masses. Plotted are the forward
667 trajectories that stay within the 30 – 50° N region for at least 3 days during the month of April
668 2009. During the spring transport from CA is dominated by strong westerly flows and air masses
669 are transported over China, Korea, and Japan and then across the Pacific, reaching North
670 America in 7 – 10 days.

671 PM arising from dust and anthropogenic emissions from CA impact the entire northern
672 hemisphere as illustrated in the hemispheric maps of seasonal average surface dust
673 concentrations due to CA emissions only (Fig. 17). The predominant westerly flows in all
674 seasons in the northern hemisphere result in the bulk of the CA emissions being transported to

675 the west. The contribution of CA sources to surface PM concentrations of 0.35 $\mu g/m^3$ or greater
676 covers large portions of the northern hemisphere, including the Arctic, all of Asia, much of
677 Europe, and portions of the continental US.

678 There are episodic and seasonal components to the intercontinental transport as shown in
679 the time series of the vertical profiles of $PM_{2.5}$ at Mt. Bachelor, Oregon (43.97N, 121.69W,
680 2700m agl) (Fig. 18). The bulk of the CA particle transport takes place in the free troposphere
681 and impacts surface concentrations in the US as the boundary layer grows and entrains "plumes"
682 aloft. This occurs most frequently in spring, summer and fall. The episodic contributions of CA
683 sources to surface concentrations can exceed $1.5\mu g/m^3$. In the fall, there is also strong transport
684 of dust from CA across Europe and out into the Atlantic.

685

686 **3.9 Future Scenarios**

687 How might PM levels change in CA over the next few decades? To address this question,
688 simulations were repeated for various emission scenarios developed and used in the
689 WMO/UNEP assessment on short-lived climate pollutants (Shindell et al., 2012) as described in
690 Sect. 2. Dust and biomass burning emissions and meteorology were the same as those used in the
691 2008/2009 simulations. The period mean changes in surface BC and $PM_{2.5}$ concentrations in
692 2030 for the reference scenario are shown in Fig. 19a, d, respectively. This scenario reflects all
693 present agreed policies affecting emissions and assumes that they are fully implemented. Under
694 this scenario $PM_{2.5}$ increases significantly in South Asia and western China (>50%) and in parts
695 of CA, including the area where the sampling sites are located. $PM_{2.5}$ decreases in Western

696 Europe and Eastern China (< 10%). BC surface concentrations show a similar pattern to $PM_{2.5}$,
697 although covering larger portions of CA with relatively larger increases in BC than in $PM_{2.5}$.
698 These results suggest that health impacts and climate warming due to BC and $PM_{2.5}$ may increase
699 in coming decades unless additional emission control measures are implemented.

700 Results for two other scenarios are also presented in Fig. 19. One scenario specifically
701 targets BC emission reductions in recognition that BC is also a major contributor to atmospheric
702 warming (Ramanathan and Carmichael, 2008). These additional measures significantly reduce
703 2030 BC concentrations by greater than 35% throughout most of the domain, with only a few
704 regions (e.g., Myanmar and eastern Afghanistan) showing increases in BC relative to 2005
705 levels. This scenario assumes that all BC emission reduction measures are perfectly implemented
706 and 100% effective. BC measures also impact emissions of co-emitted pollutants (e.g., OC and
707 SO_2). $PM_{2.5}$ concentrations under this scenario (Fig. 19e) are reduced, but by much smaller
708 amounts, and concentrations still increase relative to 2005 over large regions of South Asia and
709 western China, and parts of CA. These results suggest that health impacts in these regions may
710 increase due to the $PM_{2.5}$ increases whereas positive radiative forcing and health effects due to
711 BC may decrease. When the BC measures are used along with greenhouse gas measures aimed at
712 keeping CO_2 levels below 450 ppm, the $PM_{2.5}$ levels in South Asia are lower than 2005 levels
713 (Fig. 19f), with few exceptions (one being Myanmar region). This is due to the large decreases in
714 SO_2 and NO_x emissions under this scenario, resulting in significant reductions in particulate
715 nitrate and sulfate (e.g., a ~30% increase in particulate sulfate in CA).

716 To get a regional perspective of how the future emission changes would specifically
717 impact the CA region (See Fig. 1 for the CA region definition used in this study), we have

summarized the changes in emissions and the corresponding concentrations in Table 1. The reference 2030 emissions scenario reports an increase in emissions of BC, SO_2 and $PM_{2.5}$ over Central Asia by ~ 22, 17 and 14 % respectively w.r.t to base 2005 levels. However, the corresponding BC, SO_4 and anthropogenic portion of $PM_{2.5}$ decrease by ~ 5, 12 and 5 % respectively. This suggest that on average the concentration levels go down even though CA emissions increase due to long range transport of pollutants into CA region from the surrounding regions, but locations within CA still increase when dominated by local sources. The Low GWP emission scenario predicts decrease in BC and $PM_{2.5}$ emissions by 31% and 10% respectively with the corresponding decrease in concentrations by ~ 37% and 10 % respectively, while SO_2 emissions remained same as the reference 2030 scenario. The lowest + 450 ppm scenario shows a consistent decreasing trend in emissions and concentration of all the species. This analysis suggests that the impact of the changes in major source region emissions and their subsequent transport to Central Asia will play a major role in determining the future aerosol levels in CA.

4. Summary

AOD in CA during the period April 2008 through July 2009 averaged ~0.3 and displayed a seasonal cycle with the lowest values in the winter and highest values in spring to mid-summer with observed values of AOD > 0.6 and even > 0.8. Surface $PM_{2.5}$ measured at two sites in eastern CA averaged ~10 $\mu g/m^3$ but with large variability (hourly values from 2 - 90 $\mu g/m^3$). Surface concentrations of PM also showed a seasonal cycle with peak values and largest variability in the spring/summer, and lowest values and variability in the winter. BC at these sites averaged ~0.1 $\mu g/m^3$ with peak values (~ 1 $\mu g/m^3$) in the winter.

739 The seasonal cycles and source sector and source region contributions to PM in CA were
740 analyzed using the STEM chemical transport model. Dust was the largest component of the
741 $PM_{2.5}$ and PM_{10} mass in the region in all seasons except winter, whereas sulfate was the largest
742 anthropogenic component of the $PM_{2.5}$ mass. Dust was also found to be the major driver of the
743 seasonal cycles of AOD and PM concentrations. On an annual basis the power and industrial
744 sectors were the most important contributors to $PM_{2.5}$, while residential and transportation were
745 the most important sectors for BC. Open biomass burning within and outside the region also
746 contributed to elevated PM and BC concentrations and to the temporal variability.

747 The model simulations showed a systematic over prediction of PM mass. This is most
748 likely due in large part to the over prediction in dust. Carbonaceous PM was underpredicted and
749 it is speculated that the winter emissions associated with residential heating may be
750 underestimated in the current emissions inventory. The predicted wind speeds were biased high
751 (by ~30%) and the direction had a southwest bias. The high bias in wind speeds may also
752 contribute to the over-prediction in PM_{10}, as dust emissions depend strongly on wind speed.
753 Efforts to improve the dust emissions and to improve the wind speed and direction predictions
754 using a finer model resolution are planned. Additional efforts are needed to improve the
755 anthropogenic emissions estimates for CA.

756 Currently there are few measurements in CA that can be used to quantify the
757 intercontinental transport of pollution from Europe to Asia. The analysis of the transport
758 pathways and variations in PM mass and composition observed at the two sites in CA
759 demonstrate that this region is strategically located to characterize regional and intercontinental
760 transport of pollutants. Aerosols at these sites were shown to reflect dust, biomass burning, and

761 anthropogenic sources from South, East, and CA, Europe, and Russia depending on the time of
762 year. For example, during the spring fine particles from Europe and Africa were transported to
763 CA, on to eastern Asia, and then across the Pacific to North America.

764 Observations of PM and its composition in this region are of growing importance as it is
765 estimated that $PM_{2.5}$ levels are likely to increase significantly in Central and South Asia and
766 western China over the next few decades. Simulations for a reference 2030 emission scenario
767 showed that BC concentrations had a larger relative increase than $PM_{2.5}$ concentrations. This
768 suggests that health impacts and climate warming associated with these pollutants may increase
769 over the next decades unless additional control measures are implemented. Continued pollutant
770 observations in CA will help to characterize the changes that are rapidly taking place in the
771 region.

5. Acknowledgements

The US Environmental Protection Agency through its Office of Research and Development funded this study and collaborated in the research described here as a component of the International Science & Technology Center (ISTC) project # 3715 (Transcontinental Transport of Air Pollution from Central Asia to the US). The University of Iowa activities were also supported in part by the following grants: EPA (RD-83503701-0), NASA (NNX08AH56G), NSF (1049140), NCRR (UL1RR024979) and Fulbright-CONICYT (15093810). Its contents are solely the responsibility of the authors and do not necessarily represent the official views of the funding institutions. This manuscript has been subjected to U.S. EPA review and approved for publication. We thank all the PIs and their staff for establishing and maintaining the AERONET sites that have been used in this study. We would also like to acknowledge the Network Center for EANET and the EMEP chemical coordinating centre for the PM_{10} measurements used in this study.

6. References

Adhikary, B., Carmichael, G. R., Tang, Y., Leung, L. R., Qian, Y., Schauer, J. J., Stone, E. a., Ramanathan, V. and Ramana, M. V.: Characterization of the seasonal cycle of south Asian aerosols: A regional-scale modeling analysis, J Geophys Res, 112(D22), D22S22, doi:10.1029/2006JD008143 , 2007.

Anenberg, S. C., Schwartz, J., Shindell, D., Amann, M., Faluvegi, G., Klimont, Z., Maenhout, G., Pozzoli, L., van Dingenen, R., Vignati, E., Emberson, L., Muller, N. Z., West, J. J., Williams, M., Demkine, V., Hicks, W. K., Kuylenstierna, J., Raes, F., and Ramanathan, V.: Global air quality and health co-benefits of mitigating near-term climate change through methane and black carbon emission controls, Environ. Health Perspect., 120, 831–839, 2012.

Bates, T. S., Anderson, T. L., Baynard, T., Bond, T., Boucher, O., Carmichael, G., Clarke, A., Erlick, C., Guo, H., Horowitz, L., Howell, S., Kulkarni, S., Maring, H., McComiskey, A., Middlebrook, A., Noone, K., O'Dowd, C. D., Ogren, J., Penner, J., Quinn, P. K., Ravishankara, A. R., Savoie, D. L., Schwartz, S. E., Shinozuka, Y., Tang, Y., Weber, R. J., and Wu, Y.: Aerosol direct radiative effects over the northwest Atlantic, northwest Pacific, and North Indian Oceans: estimates based on in-situ chemical and optical measurements and chemical transport modeling, Atmos. Chem. Phys., 6, 1657-1732, doi:10.5194/acp-6-1657-2006, 2006.

Bauer, S., D. Koch, N. Unger, S. M. Metzger, D. T. Shindell, and D. G. Streets: Nitrate aerosols today and in 2030: a global simulation including aerosols and tropospheric ozone, Atmos. Chem. Phys., 7, 5043–5059, 2007

Carmichael, G. R., Adhikary, B., Kulkarni, S., D'Allura, A., Tang, Y., Streets, D., Zhang, Q., Bond, T. C., Ramanathan, V., Jamroensan, A., and Marrapu, P.: Asian aerosols: current and year 2030 distributions and implications to human health and regional climate change, Environ. Sci. Technol., 43, 5811–5817, 2009.

811 Chen, B., Sverdlik, L. G., Imashev, S. A., Solomon, P. A., Lantz, J., Schauer, J. J., Shafer, M.
812 M., Artamonova, M. S., and Carmichael, G.: Empirical relationship between particulate matter
813 and aerosol optical depth over Northern Tien-Shan, Central Asia, Air Quality, Atmosphere &
814 Health, 6.2, 358-396, doi: 10.1007/s11869-012-0192-5, 2012.
815

816 Chen, B. B., Imashev, S. A., Sverdlik, L. G., Solomon, P. A., Lantz, J., Schauer, J. J., Shafer, M.
817 M., Artamonova, M. S. and Carmichael, G. R.: Ozone Variations over Central Tien-Shan in
818 Central Asia and Implications for Regional Emissions Reduction Strategies, Aerosol Air Qual
819 Res, 13, 555–562 Available from: 10.4209/aaqr.2012.06.156, 2013.

820 Chung, C. E., Ramanathan, V., Carmichael, G., Kulkarni, S., Tang, Y., Adhikary, B., Leung, L.
821 R. and Qian, Y.: Anthropogenic aerosol radiative forcing in Asia derived from regional models
822 with atmospheric and aerosol data assimilation, Atmos Chem Phys, 10(13), 6007–6024,
823 doi:10.5194/acp-10-6007-2010, 2010.

824 D'Allura, A., Kulkarni, S., 5 Carmichael, G. R., Finardi, S., Adhikary, B., Wei, C., Streets, D.,
825 Zhang, Q., Pierce, R. B., Al-Saadi, J. A., Diskin, G., Wennberg, P.: Meteorological and air
826 quality forecasting using the WRF–STEM model during the 2008 ARCTAS field campaign,
827 Atmos. Environ., 45, 6901–6910, doi:10.1016/j.atmosenv.2011.02.073, 2011.

828 Denier van der Gon, H., Visschedijk, A., Droge, R., Mulder, M., Johansson, C., and Klimont, Z.:
829 A high resolution emission inventory of particulate elemental carbon and organic carbon for
830 Europe in 2005, 7th International Conference on Air Quality – Science and Application (Air
831 Quality 2009), Istanbul, 2009.

832 Emerson, J. W., Hsu, A., Levy, M. A., de Sherbinin, A., Mara, V., Esty, D. C., and Jaiteh, M.:
833 Environmental Performance Index and Pilot Trend Environmental Performance Index, Yale
834 Center for Environmental Law and Policy, New Haven, 2012

835 Freitas, S. R., Longo, K. M., Chatfield, R., Latham, D., Silva Dias, M. A. F., Andreae, M. O.,
836 Prins, E., Santos, J. C., Gielow, R. and Carvalho Jr., J. A.: Including the sub-grid scale plume
837 rise of vegetation fires in low resolution atmospheric transport models, Atmos Chem Phys ,
838 7(13), 3385–3398, doi:10.5194/acp-7-3385-2007 , 2007.

839 Freitas, S. R., Longo, K. M., Trentmann, J. and Latham, D.: Technical Note: Sensitivity of 1-D
840 smoke plume rise models to the inclusion of environmental wind drag, Atmos Chem Phys, 10(2),
841 585–594, doi:10.5194/acp-10-585-2010, 2010.

842 Ginoux, P., Chin, M., Tegen, I., Prospero, J. M., Holben, B., Dubovik, O. and Lin, S.-J.: Sources
843 and distributions of dust aerosols simulated with the GOCART model, J Geophys Res-Atmos,
844 106(D17), 20255–20273, doi:10.1029/2000JD000053, 2001.

845 Gong, S. L.: A parameterization of sea-salt aerosol source function for sub- and super-micron
846 particles, Global Biogeochem. Cy. , 17(4), 1097, doi:10.1029/2003GB002079 , 2003.

847 Grell, G. A., Peckham, S. E., Schmitz, R., McKeen, S. A., Frost, G., Skamarock, W. C., and
848 Eder, B.: Fully coupled “online” chemistry within the WRF model, Atmos. Environ. 39, 6957–
849 6975, 2005.

850 Grell, G., Freitas, S. R., Stuefer, M., and Fast, J.: Inclusion of biomass burning in WRF-Chem:
851 impact of wildfires on weather forecasts, Atmos. Chem. Phys., 11, 5289–5303, doi:10.5194/acp-
852 11-5289-2011, 2011.

853 Guttikunda, S., Tang, Y., Carmichael, G., Kurata, G., Pan, L., Streets, D., Woo, J.-H.,
854 Thongboonchoo, N., and Fried, A.: Impacts of Asian megacity emissions on regional air quality
855 during spring 2001, J. Geophys. Res., 110, D20301, doi:10.1029/2004JD004921, 2005.

856 Hsu, N. C., Tsay, S.-C., King, M. D. and Herman, J. R.: Aerosol properties over bright-reflecting
857 source regions, IEEE T Geosci Remote , 42(3), 557–569, doi:10.1109/TGRS.2004.824067,
858 2004.

859 Hsu, N. C., Tsay, S.-C., King, M. D. and Herman, J. R.: Deep Blue Retrievals of Asian Aerosol
860 Properties During ACE-Asia, IEEE T Geosci Remote , 44(11), 3180–3195,
861 doi:10.1109/TGRS.2006.879540, 2006.

862 Huang, M., G. Carmichael, S. Kulkarni, D. Streets, Z. Lu, Q. Zhang, B. Pierce, Y. Kondo, J.
863 Jimenez-Palacios, M. J. Cubison, B. E. Anderson, and A. Wisthaler: Sectoral and geographical
864 contributions to summertime continental United States (CONUS) black carbon spatial
865 distributions, *Atmos. Environ., 51*, 165-174, doi:10.1016/j.atmosenv.2012.01.021,2012

866 HTAP: Hemispheric Transport of Air Pollution 2010 (Executive Summary). Available online
867 from: http://www.htap.org/publications/2010_report/2010_Final_Report/EBMeeting2010.pdf
868 (Accessed 26 February 2013), 2010.

869 Hubanks, P. A., King, M. A., Platnick, S., and Pincus, R.: MODIS atmosphere L3 gridded
870 product algorithm theoretical basis document, MODIS Algorithm Teoretical Basis Document
871 No. ATBD-MOD-30 ,available at: http://modis-
872 atmos.gsfc.nasa.gov/_docs/L3_ATBD_2008_12_04.pdf,2008.

873 Kurata, G., Carmichael, G. R., Streets, D. G., Kitada, T., Tang,Y., Woo, J. H., and
874 Thongboonchoo, N.: Relationships between emission sources and air mass characteristics in East
875 Asia during the TRACE-P period, Atmos. Environ., 38(40), 6977–6987, 2004.

876 Levy, R. C., Remer, L. A., Mattoo, S., Vermote, E. F. and Kaufman, Y. J.: Second-generation
877 operational algorithm: Retrieval of aerosol properties over land from inversion of Moderate
878 Resolution Imaging Spectroradiometer spectral reflectance, J Geophys Res-Atmos , 112(D13),
879 D13211, doi:10.1029/2006JD007811, 2007.

880 Lu, Z., Zhang, Q. and Streets, D. G.: Sulfur dioxide and primary carbonaceous aerosol emissions
881 in China and India, 1996–2010, Atmos Chem Phys, 11(18), 9839–9864, doi:10.5194/acp-11-
882 9839-2011 Available online from: http://www.atmos-chem-phys.net/11/9839/2011/), 2011.

883 Miller-Schulze, J. P., Shafer, M. M., Schauer, J. J., Solomon, P. a., Lantz, J., Artamonova, M.,
884 Chen, B., Imashev, S., Sverdlik, L., Carmichael, G. R. and Deminter, J. T.: Characteristics of
885 fine particle carbonaceous aerosol at two remote sites in Central Asia, Atmos Environ, 45(38),
886 6955–6964, doi:10.1016/j.atmosenv.2011.09.026, 2011.

887 Park, S., Martin M. Shafer, James J. Schauer, Paul A. Solomon, Jeffrey Lantz, Maria
888 Artamonova, Boris Chen, Sanjar Imashev, Leonid Sverdlik, Greg R. Carmichael: Chemical
889 characteristics, dynamics and provenance of mineral dust observed at two sites in Central Asia,
890 Atmos. Environ., in preparation,2014.

891 Ramanathan, V. and Carmichael, G.: Global and regional climate changes due to black carbon,
892 Nat Geosci, 1(4), 221–227 Available online from:
893 http://www.nature.com/ngeo/journal/vaop/ncurrent/full/ngeo156.html (Accessed 18 February
894 2013), 2008.

895 Remer, L. A., Kaufman, Y. J., Tanré, D., Mattoo, S., Chu, D. A., Martins, J. V, Li, R.-R., Ichoku,
896 C., Levy, R. C., Kleidman, R. G., Eck, T. F., Vermote, E., and Holben, B.N.: The MODIS
897 aerosol algorithm products and validation, J. Atmos. Sci., 62, 947–973, doi:10.1175/JAS3385.1,
898 2005.

899 Skamarock, W. C., Klemp, J. B., Dudhia, J., Gill, D. O., Barker, D. M., Duda, M. G., Huang,
900 X.- Y., Wang, W., and Powers, J. G.: A Description of the Advanced Research WRF, Version 3.
901 Technical Report NCAR/TN475+ST R. National Center for Atmospheric Research Technical
902 Note, Boulder, Colorado, 2008.

903 Shindell, D., Kuylenstierna, J. C. I., Vignati, E., van Dingenen,R., Amann, M., Klimont, Z.,
904 Anenberg, S. C., Muller, N.,Janssens-Maenhout, G., Raes, F., Schwartz, J., Faluvegi, G.,Pozzoli,
905 L, Kupiainen, K., Hoglund-Isaksson, L., Emberson, L., Streets, D., Ramanathan, V., Hicks, K.,
906 Kim Oanh, N. T., Milly, G., Williams, M., Demkine, V., and Fowler, D: Simultaneously
907 mitigating near-term climate change and improving human health and food security, Science,
908 335, 183–189, doi:10.1126/science.1210026 , 2012.

909 UNEP: Framework Convention on Environmental Protection for Sustainable Development in
910 Central Asia, Regional Resource Centre for Asia and the Pacific (PRC.AP), available at:
911 http://www.rrcap.ait.asia/library/ca-report/Brief-Convention.doc, (last access: 25 April 2014),
912 2006.

913 UNEP and WMO: Integrated Assessment of Black Carbon and Tropospheric Ozone: Summary
914 for Decision Makers. available at:
915 http://www.unep.org/dewa/Portals/67/pdf/BlackCarbon_SDM.pdf (last access: 26 February
916 2013), 2011.

Uno, I., Satake, S., Carmichael, G. R., Tang, Y., Wang, Z., Takemura, T., Sugimoto, N., Shimizu, A., Murayama, T., Cahill, T.A., Cliff, S., Uematsu, M., Ohta, S., Quinn, P. K., and Bates, T.S.: Numerical study of Asian dust transport during the springtime of 2001 simulated with the Chemical Weather Forecasting System (CFORS) model, J. Geophys. Res., 109(D19S24), doi:10.1029/2003JD004222, 2004.

V Visschedijk, A., Denier van der Gon, H., Droge, R.,van der Brugh, H.: A European high resolution and size-differentiated emission inventory for elemental and organic carbon for the year 2005, TNO-034-UT-2009-00688_RPT-ML, TNO, Utrecht, 2009

Wang, W., Bruyere, C., Duda, M., Dudhia, J., Gill, D., Lin, H.-C., Michalakes, J., Rizvi, S. and Zhang, X.: Version 3 Modeling System User ' s Guide January 2011, National Center for Atmospheric Research (NCAR), available at: http://www.mmm.ucar.edu/wrf/users/docs/user_guide_V3.2/ARWUsersGuideV3.pdf (last access: 25 April 2014), 2011.

Wesely, M. L. and Hicks, B. B.: A review of the current status of knowledge on dry deposition, Atmos Environ, 34(12–14), 2261–2282, doi:http://dx.doi.org/10.1016/S1352-2310(99)00467-7, 2000.

Whish-Wilson, P.: The Aral Sea environmental health crisis the desiccation of the Aral Sea health in the Aral Sea region, Journal of Rural and Remote Environmental Health,1(2), 29–34, available at: http://www.jcu.edu.au/jrtph/vol/v01whish.pdf (last access: 25 April 2014), 2002.

Wiedinmyer, C., Akagi, S. K., Yokelson, R. J., Emmons, L. K., Al-Saadi, J. a., Orlando, J. J. and Soja, a. J.: The Fire INventory from NCAR (FINN): a high resolution global model to estimate the emissions from open burning, Geoscientific Model Development, 4(3), 625–641, doi:10.5194/gmd-4-625-2011, 2011.

Zhang, Q., Streets, D. G., Carmichael, G. R., He, K. B., Huo, H., Kannari, A., Klimont, Z., Park, I. S., Reddy, S., Fu, J. S., Chen, D., et al.: Asian emissions in 2006 for the NASA INTEX-B mission., Atmos Chem Phys, 9(14/2), 5131–5153, doi:10.5194/acp-9-5131-2009, 2009.

7. Table Captions

Table:1 Summary of changes in Central Asia (CA) region (See figure 1 for CA region definition) emissions and concentration under the future emission scenarios (See Sect. 3.9 for more details)

8. Figure Captions

Fig. 1. WRF-STEM modeling domain set up and source region definition used in the simulations. Modeling analysis was done on the hemispheric scale. The black dotted rectangular box denotes the subset of the modeling domain used in this analysis. The triangle and circle markers denote locations of the LST and Bishkek observation sites. The anthropogenic source regions are denoted by colored regions with the A notation: A1 (N. America), A2 (Europe), A3 (Russia), A4 (Middle East), A5 (Central Asia), A6 (China) and A7 (South + Southeast Asia). The dust source regions are indicated by the magenta rectangles with the D notations: D1 (Africa), D2 (Middle East), D3 (Central Asia) and D4 (Western China). The biomass burning sources regional boundaries are indicated by the long dashed black lines with B notations: B1 (N. America i.e. region west of 25 W), B2 (Europe i.e. region west of 45E and 40 N and above), B3 (Siberia : i.e east of 45 E and 40 N and above) and B4 (South Asia i.e. below 40 N). The insert shows the topography around the observation sites.

Fig. 2. Spatial distribution of a) BC b) SO_2 c) Natural dust d) Biomass burning $PM_{2.5}$ emissions averaged over the simulation period in Gg/yr/grid.

Fig. 3 Spatial distribution of (a) MODIS and (b) modeled AOD along with (c) Comparison of MODIS, AERONET and Simulated AOD shown as box whisker plots averaged over the simulation period. The box plots are based on data that are paired in time and space (See Sect. 3.2.1 for more details). The triangle and circle markers on the spatial plots denote the location of LST and Bishkek sites. The numbers on the map denote contour values at sharp gradients. In each box whisker panel, the middle line denotes the median value, while the edges of the box represent 25th and 75th percentile values respectively. The whiskers denote the maximum and minimum values.

Fig. 4. Spatial distribution of simulated a) BC ($\mu g/m^3$), b) Dust ($\mu g/m^3$), c) $PM_{2.5}$ ($\mu g/m^3$), and d) $PM_{2.5}/PM_{10}$ ratio averaged over the simulation period. The values on the map denote contour values at sharp gradients.

Fig. 5. Comparison of predicted meteorological variables from WRF model with observations shown as box and whisker plots over the simulation period (a) Temperature (K), (b) Relative Humidity RH (%), (c) Wind Speed (m/s), (d) Wind Direction (°), and (e) PBL height (m). Lidar denotes the LST (Lidar Station Teplokluchenka) site. In each box whisker panel, the middle line denotes the median value, while the edges of the box represent 25th and 75th percentile values respectively. The whiskers denote the maximum and minimum values.

Fig. 6. Comparison of predicted aerosols with observations shown as box and whisker plots over the simulation period at a) LST and b) Bishkek sites. SP and LE denote the AOD from the sun-photometer (SP) and integrated fromthe vertical extinction profiles (LE). OBS and TEOM denote filter and TEOM measurements while the MDL denotes the modeled values respectively. Lidar denotes the LST (Lidar Station Teplokluchenka) site. In each box whisker panel, the middle line denotes the median value, while the edges of the box represent 25th and 75th percentile values respectively. The whiskers denote the maximum and minimum values. The triangle marker denotes the mean value.

Fig. 7. Summary of period mean contributions by source regions and sectors for AOD, $PM_{2.5}$, dust, non-dust $PM_{2.5}$, sulfate and BC in % for the grid cells containing the Bishkek and LST

observation sites, and spatially averaged over the Central Asia region. See Fig. 1 for anthropogenic, dust and fire source regions. Lidar denotes the LST (Lidar Station Teplokluchenka) site.

Fig. 8. Temporal variability in simulated AOD compared with observations at the LST site. The box-plots of monthly values are shown. AOD from the sun-photometer (SP) and integrated from the vertical extinction profiles (LE) are shown. MDL denotes modeled values. Lidar denotes the LST (Lidar Station Teplokluchenka) site. In each box whisker panel, the middle line denotes the median value, while the edges of the box represent 25th and 75th percentile values respectively. The whiskers denote the maximum and minimum values.

Fig. 9. Comparison of simulated PM mass with filter-based observations at Central Asia sites (a) $PM_{2.5}$ (LST) along with TEOM non-volatile measurements, (b) $PM_{2.5}$ (Bishkek), (c) PM_{10} (LST), and (d) PM_{10} (Bishkek) in ($\mu g/m^3$). Lidar denotes the LST (Lidar Station Teplokluchenka) site.

Fig. 10. Temporal variability in simulated (a) Temperature (K) and (b) Relative Humidity RH (%) from WRF model compared with observations at the LST and Bishkek sites. Lidar denotes the LST (Lidar Station Teplokluchenka) site.

Fig. 11. Simulated composition of $PM_{2.5}$ at the LST site by a) Species ($\mu g/m^3$), b) Fine dust source regions($\mu g/m^3$) c) Anthropogenic $PM_{2.5}$ source regions ($\mu g/m^3$) d) Anthropogenic $PM_{2.5}$ source ($\mu g/m^3$) e) Biomass $PM_{2.5}$ source regions($\mu g/m^3$).The contributions from source region and sectors denote the non – dust portion of $PM_{2.5}$ mass.

Fig. 12. Simulated composition of BC at the LST site by a) Source regions ($\mu g/m^3$), b) Source sector ($\mu g/m^3$), and c) Biomass burning source regions ($\mu g/m^3$).

Fig. 13. Time altitude cross sections of weekly averaged predicted BC, dust and $PM_{2.5}$ for the simulation period at the LST site. The numbers denote the specific episodes of aerosol enhancements for back trajectory analysis in Fig. 14 and Fig. 15. Lidar denotes the LST (Lidar Station Teplokluchenka) site.

Fig. 14. Ten day air mass back trajectories for August 2008 (events 1 and 2 as denoted in Fig. 13) color coded by source regions. The blue diamond and green square hatched areas denote the natural dust and biomass burning emission sources while the number in black denote MODIS AOD contours averaged over the event time period and ten day prior time window. The trajectories are color coded by source regions including Africa (blue), Middle East (green), Central Asia (yellow), North Asia biomass (> 50° N, black), Europe (brown), China (red) and South Asia (orange). Lidar denotes the LST (Lidar Station Teplokluchenka) site.

Fig. 15. Same as Fig. 14 but for November 2008, January 2009 and April 2009 (events 3, 4, 5 denoted in Fig. 13).

Fig. 16 Ten day air mass forward trajectories illustrating the seasonality in transport pathways out of CA for a) June 2008, b) December 2008, and c) April 2009. The blue diamond, green square hatched areas denote the natural dust and biomass burning emission sources while the number in black denote MODIS AOD contours, respectively, averaged over the event time

period and subsequent ten day time window. Lidar denotes the LST (Lidar Station Teplokluchenka) site.

Fig. 17. Seasonally averaged surface total dust (PM_{10}) concentrations from Central Asia dust emissions. DJF (top left panel) denotes the average for the months of December, January and February. MAM (top right panel) denotes the average for months of March, April and May. JJA (bottom left panel) denotes the average for months of June, July and August while SON (bottom right panel) denotes average for months of September, October and November.

Fig. 18. Time series of predicted surface concentration at 6 h time step (top panel) and weekly averaged time altitude cross sections (bottom panel) of total dust (PM_{10}) from Central Asia dust emissions at Mt. Bachelor, Oregon.

Fig. 19. Percent change in simulated period mean surface BC and $PM_{2.5}$ concentrations for future 2030 emission scenarios relative to the base year (2005) a),d) reference 2030, a),e) BC measures (low) and c),f) BC (lowest) and greenhouse gas measures aimed at keeping CO_2 levels below 450 ppm. Refer to Sec. 2.3 for more details on emission scenarios.

9. Supplemental Materials Figure and Table Captions

Table S1. List of Sites from AERONET, EANET and EMEP used in this study (See Sect. 3.2 for details)

Table S2. Statistical summary of comparison of regional average MODIS and modeled AOD over selected source regions including CA, China, Europe, Middle East, Russia and South Asia . (See Fig 1 and Sect.3.2 for more details)

Table S3. Comparison of the observed and predicted surface meteorology at the observation sites.

Table S4. Comparison of observations and model of AOD, $PM_{2.5,}$ PM_{10}, BC and OC at the LST and Bishkek sites.

Fig. S1. Seasonal variability in spatial distribution of biomass burning $PM_{2.5}$ emissions in Gg/month/grid (a) April 2008, (b) August 2008, (c) November 2008, and (d) May 2009.

Fig. S2. Spatial distribution of a) base year 2005 BC emissions (Gg/yr/grid) along with percent change (w.r.t to base year 2005) in b) Reference 2030 BC emissions c) 2030 BC emissions with BC measures (low) and d) 2030 BC emissions with BC (lowest) and greenhouse gas measures aimed at keeping CO_2 levels below 450ppm. The triangle and circle markers denote locations of the LST and Bishkek sites. Refer to Sec. 2.3 for more details on emission scenarios.

Fig. S3. Spatial distribution of a) base year 2005 $PM_{2.5}$ emissions (Gg/yr/grid) along with percent change (w.r.t to base year 2005) in b) Reference 2030 $PM_{2.5}$ emissions c) 2030 $PM_{2.5}$ emissions with BC measures and d) 2030 $PM_{2.5}$ emissions with BC and greenhouse gas measures aimed at

keeping CO_2 levels below 450ppm. The triangle and circle markers denote locations of the LST and Bishkek sites. Refer to Sec. 2.3 for more details on emission scenarios.

Fig. S4. Spatial distribution of a) base year 2005 SO_2 emissions (Gg/yr/grid) along with percent change (w.r.t to base year 2005) in (b) Reference 2030 SO_2emissions c) 2030 SO_2 emissions with BC measures and d) 2030 SO_2 emissions with BC and greenhouse gas measures aimed at keeping CO_2 levels below 450ppm. The triangle and circle markers denote locations of the LST and Bishkek sites. Refer to Sec. 2.3 for more details on emission scenarios.

Fig. S5. Comparison of regional average AOD from MODIS with simulated values shown as box plots over the simulation period for selected source regions including Central Asia, China, Europe, Middle East, Russia and South Asia. (See Fig 1 and Sect.3.2 for more details)

Fig. S6. Comparison of regional average AOD from MODIS with simulated values shown as monthly box plots over the simulation period for selected source regions (a) Central Asia (b) Middle East (c) Europe (d) China (e) South Asia and (f) Russia (See Fig 1 and Sect.3.2 for more details)

Fig. S7. Comparison of predict PM_{10} with monthly observations from the European Monitoring and Evaluation Programme (EMEP available at http://www.nilu.no/projects/ccc/emepdata.html) and the Acid Deposition Monitoring Network in East Asia (EANET available at http://www.eanet.asia/product/index.html) surface site networks shown as box and whisker plots over the simulation period In each box whisker panel, the middle line denotes the median value, while the edges of the box represent 25th and 75th percentile values respectively. The whiskers denote the maximum and minimum values.

Fig. S8. Comparison of observed and predicted PBL heights (m) at the LST site. Observed PBL heights were determined from the Lidar profiles.

Fig. S9. Spatial distribution of predicted species contributions (%) to AOD averaged over the simulation period a) Carbonaceous aerosols (BC+OC), b) SO4, c) Other PM, and d) Dust.

Fig. S10. Spatial distribution of predicted species contributions (%) to $PM_{2.5}$ averaged over the simulation period a) Carbonaceous aerosols (BC+OC), b) SO4, c) Other $PM_{2.5}$, and d) Dust.

Fig. S11. Seasonal variability in spatial distribution of MODIS and simulated AOD averaged over the simulation period.

Fig S12. Summary of period mean contributions by source regions and sectors for OC in % for the grid cells containing the Bishkek and LST observation sites, and spatially averaged over the Central Asia region. See Fig. 1 for anthropogenic and fire source regions.

Table:1 Summary of changes in Central Asia (CA) region (See figure 1 for CA region definition) emissions and concentration under the future emission scenarios (See Sect. 3.9 for more details)

Emission Scenario	**Emissions Gg yr^{-1}**			**Emissions change (%) w.r.t to base 2005**		
	BC	SO_2	PM_{25}	BC	SO_2	PM_{25}
Base 2005	39	1130	197			
Reference 2030	47	1326	224	22.1	17.3	13.9
Low GWP 2030	27	1325	177	-31.1	17.3	-10.1
Lowest GWP + 450	21	1058	115	-46.9	-6.4	-41.5

	Concentration (µg m^{-3})			**Concentration change (%) w.r.t to base 2005**		
	BC	SO_4	PM_{25}	BC	SO_4	$PM_{2.5}$
Base 2005	0.17	3.04	4.26			
Reference 2030	0.16	2.65	4.03	-4.2	-12.6	-5.3
Low GWP 2030	0.11	2.64	3.85	-36.6	-13	-9.5
Lowest GWP + 450	0.10	2.04	3.06	-38.5	-32.9	-28

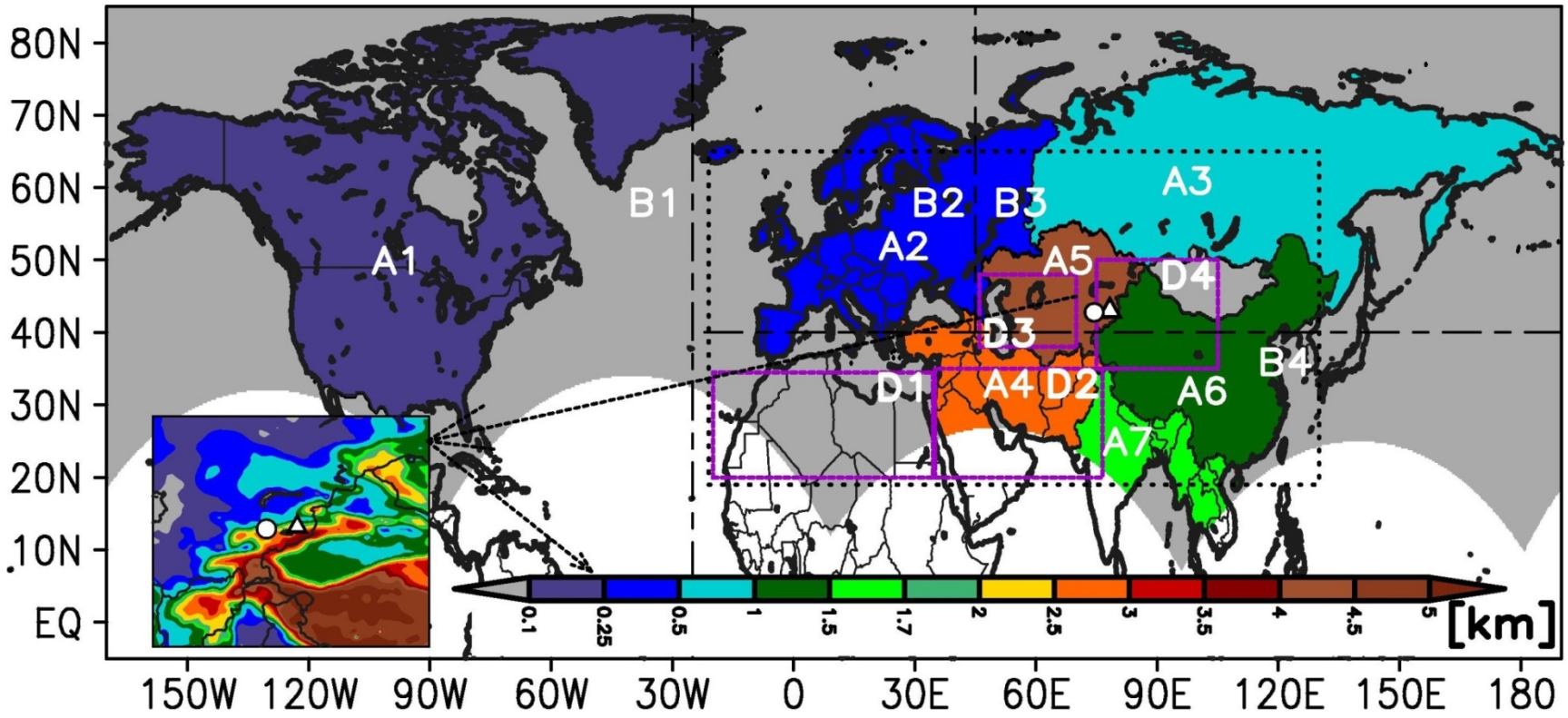

Fig. 1. WRF-STEM modeling domain set up and source region definition used in the simulations. Modeling analysis was done on the hemispheric scale. The black dotted rectangular box denotes the subset of the modeling domain used in this analysis. The triangle and circle markers denote locations of the LST and Bishkek observation sites. The anthropogenic source regions are denoted by colored regions with the A notation: A1 (N. America), A2 (Europe), A3 (Russia), A4 (Middle East), A5 (Central Asia), A6 (China) and A7 (South + Southeast Asia). The dust source regions are indicated by the magenta rectangles with the D notations: D1 (Africa), D2 (Middle East), D3 (Central Asia) and D4 (Western China). The biomass burning sources regional boundaries are indicated by the long dashed black lines with B notations: B1 (N. America i.e. region west of 25 W), B2 (Europe i.e. region west of 45E and 40 N and above), B3 (Siberia : i.e east of 45 E and 40 N and above) and B4 (South Asia i.e. below 40 N). The insert shows the topography around the observation sites.

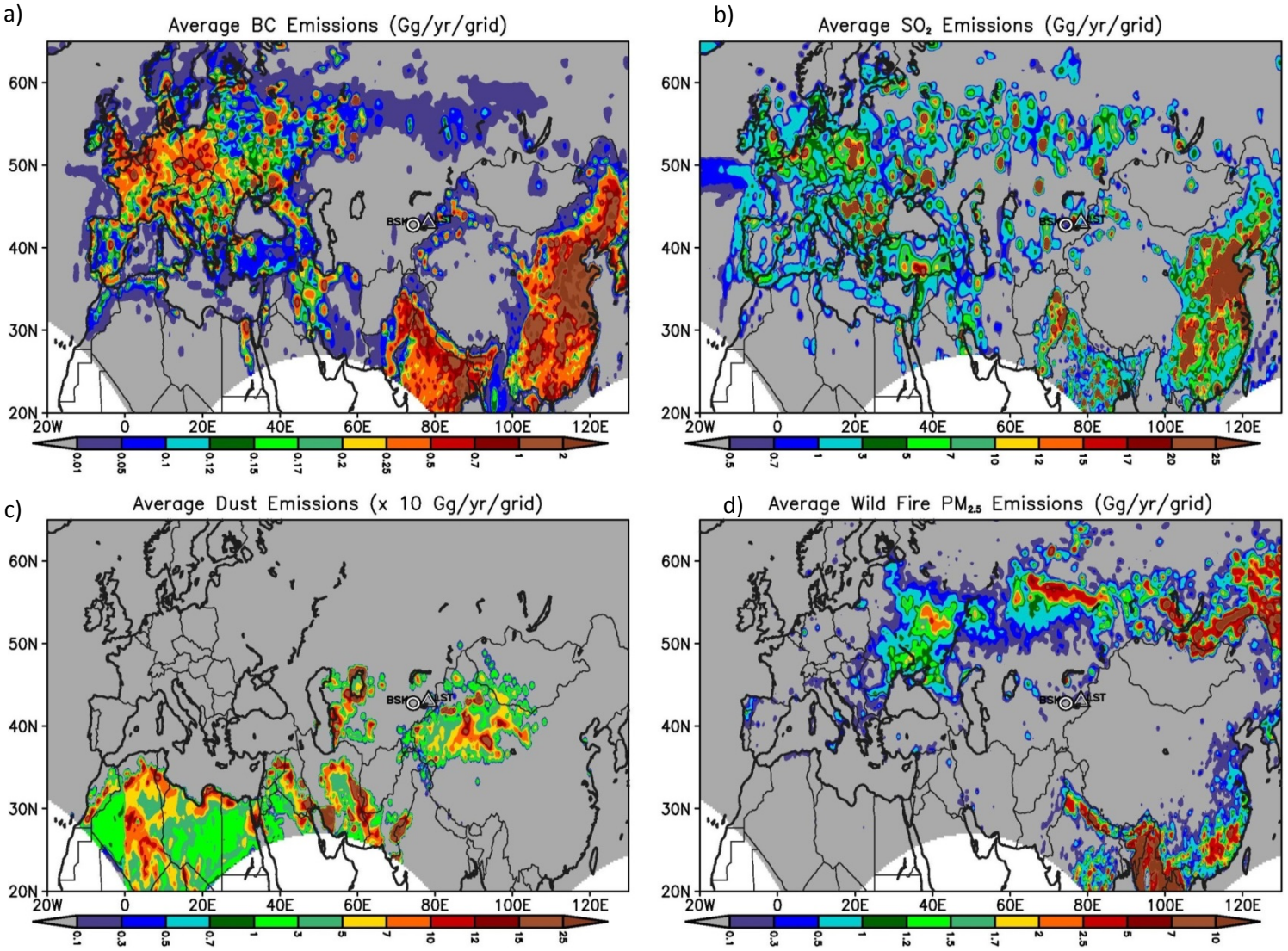

Fig. 2. Spatial distribution of a) BC b) SO_2 c) Natural dust d) Biomass burning $PM_{2.5}$ emissions averaged over the simulation period in Gg/yr/grid.

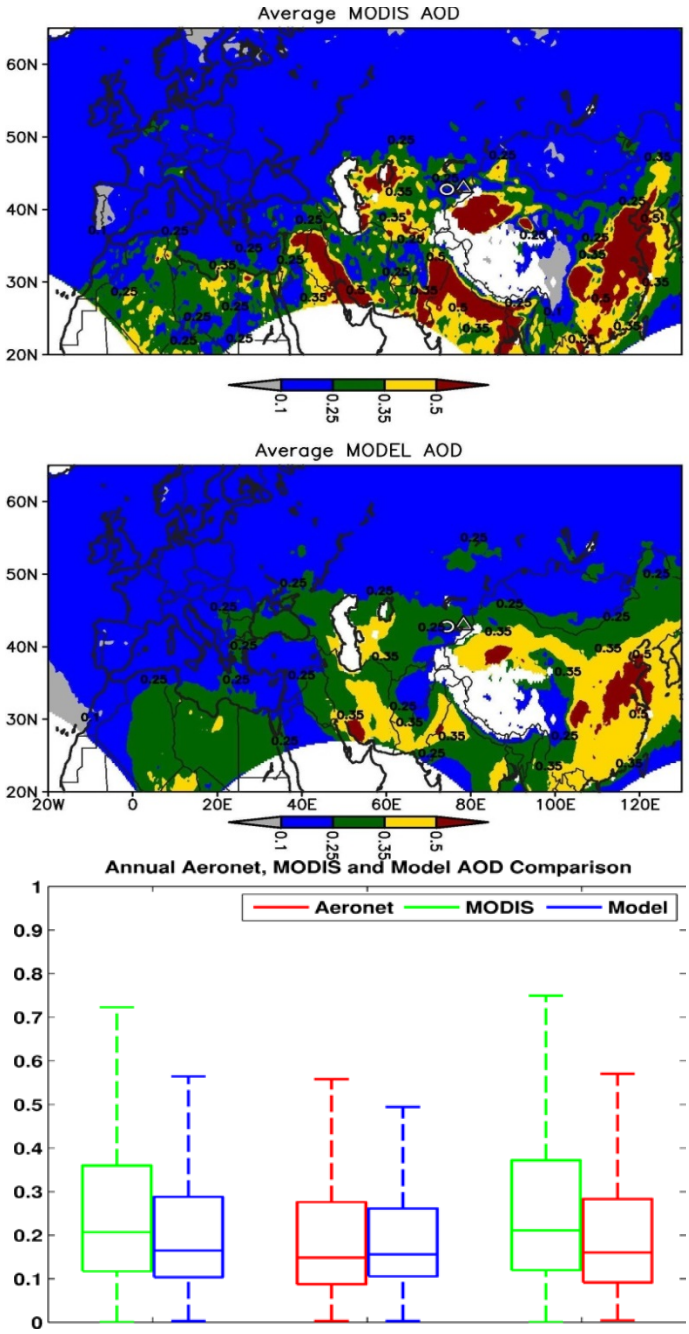

Fig. 3 Spatial distribution of (a) MODIS and (b) modeled AOD along with (c) Comparison of MODIS, AERONET and Simulated AOD shown as box whisker plots averaged over the simulation period. The box plots are based on data that are paired in time and space (See Sect. 3.2.1 for more details). The triangle and circle markers on the spatial plots denote the location of LST and Bishkek sites. The numbers on the map denote contour values at sharp gradients. In each box whisker panel, the middle line denotes the median value, while the edges of the box represent 25th and 75th percentile values respectively. The whiskers denote the maximum and minimum values.

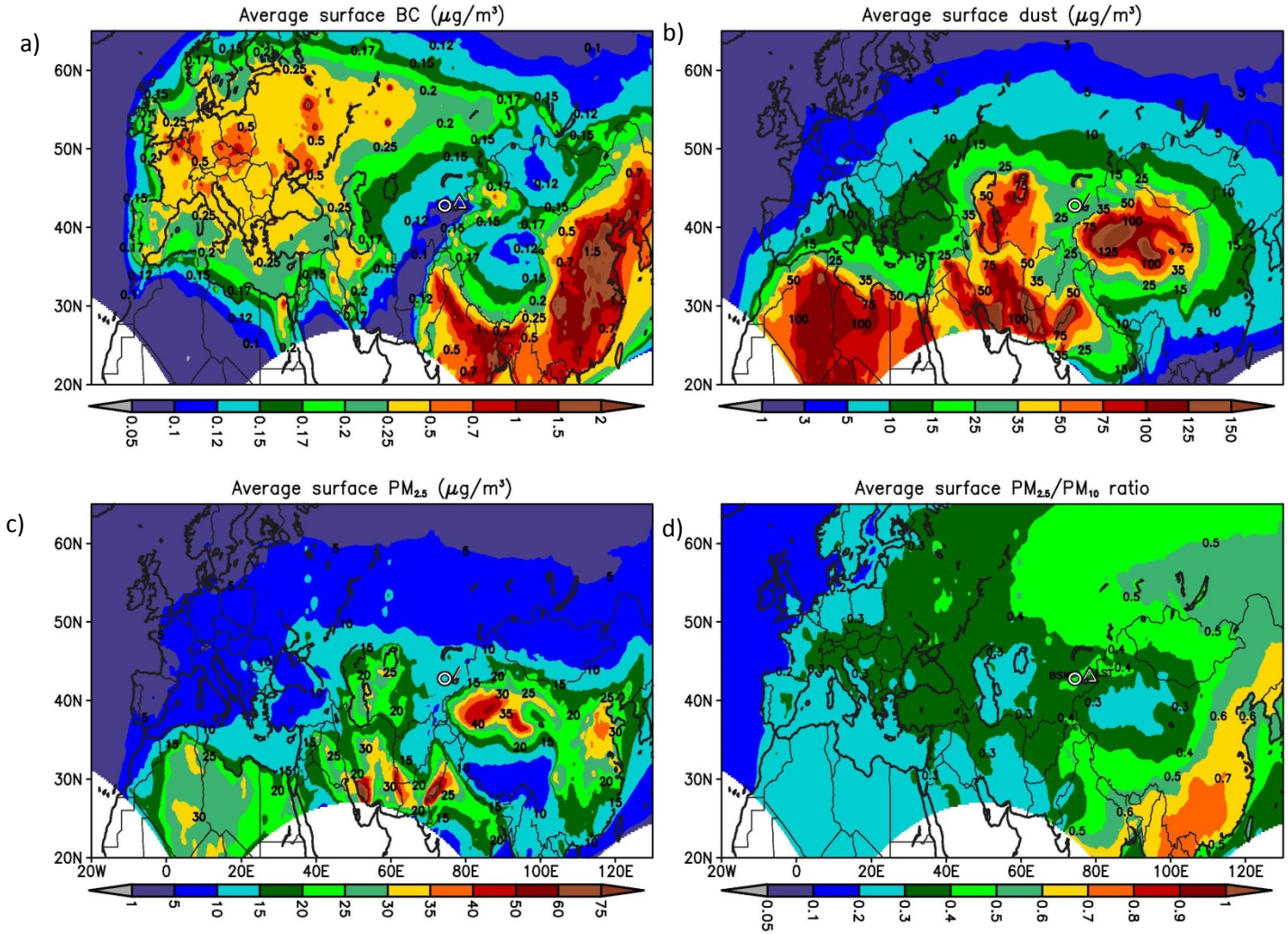

Fig. 4. Spatial distribution of simulated a) BC (μg/m^3), b) Dust (μg/m^3), c) $PM_{2.5}$ (μg/m^3), and d) $PM_{2.5}/PM_{10}$ ratio averaged over the simulation period. The values on the map denote contour values at sharp gradients.

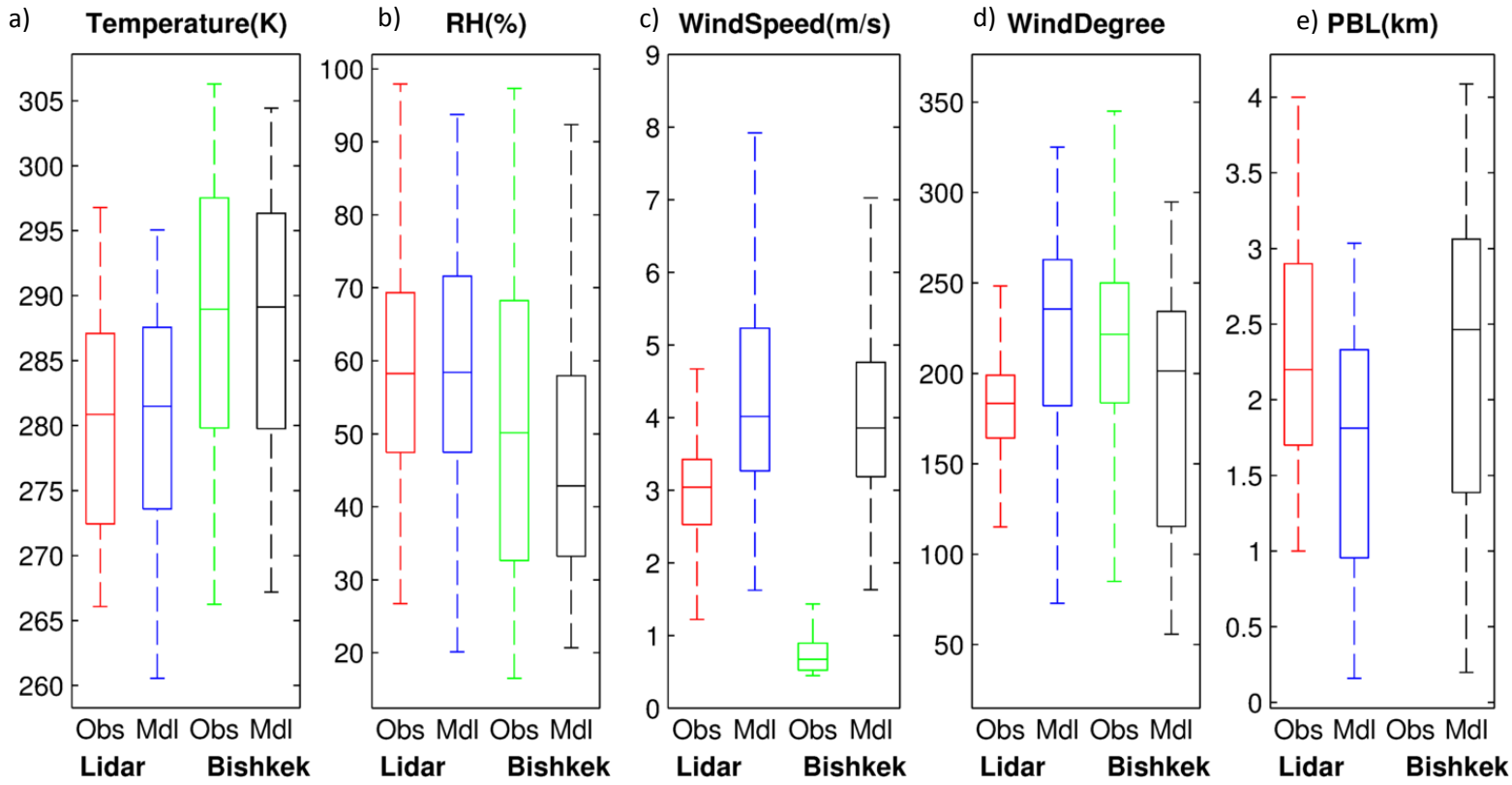

Fig. 5. Comparison of predicted meteorological variables from WRF model with observations shown as box and whisker plots over the simulation period (a) Temperature (K), (b) Relative Humidity RH (%), (c) Wind Speed (m/s), d) Wind Direction (°), and PBL height (m). Lidar denotes the LST (Lidar Station Teplokluchenka) site. In each box whisker panel, the middle line denotes the median value, while the edges of the box represent 25th and 75th percentile values respectively. The whiskers denote the maximum and minimum values.

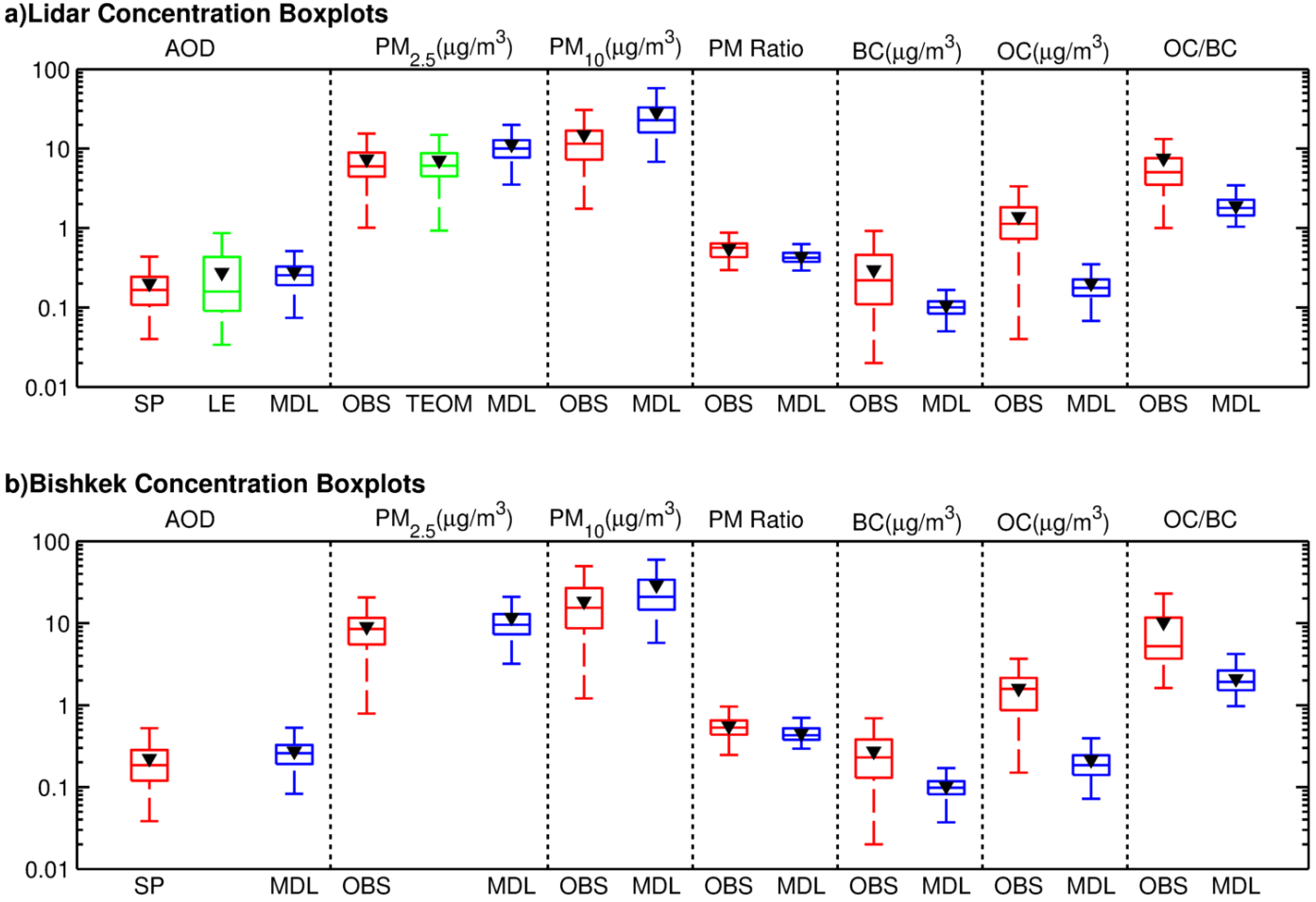

Fig. 6. Comparison of predicted aerosols with observations shown as box and whisker plots over the simulation period at a) LST and b) Bishkek sites.SP and LE denote the AOD from the sun-photometer (SP) and integrated from the vertical extinction profiles (LE). OBS and TEOM denote filter and TEOM measurements while the MDL denotes the modeled values respectively. Lidar denotes the LST (Lidar Station Teplokluchenka) site. In each box whisker panel, the middle line denotes the median value, while the edges of the box represent 25th and 75th percentile values respectively. The whiskers denote the maximum and minimum values. The triangle marker denotes the mean value.

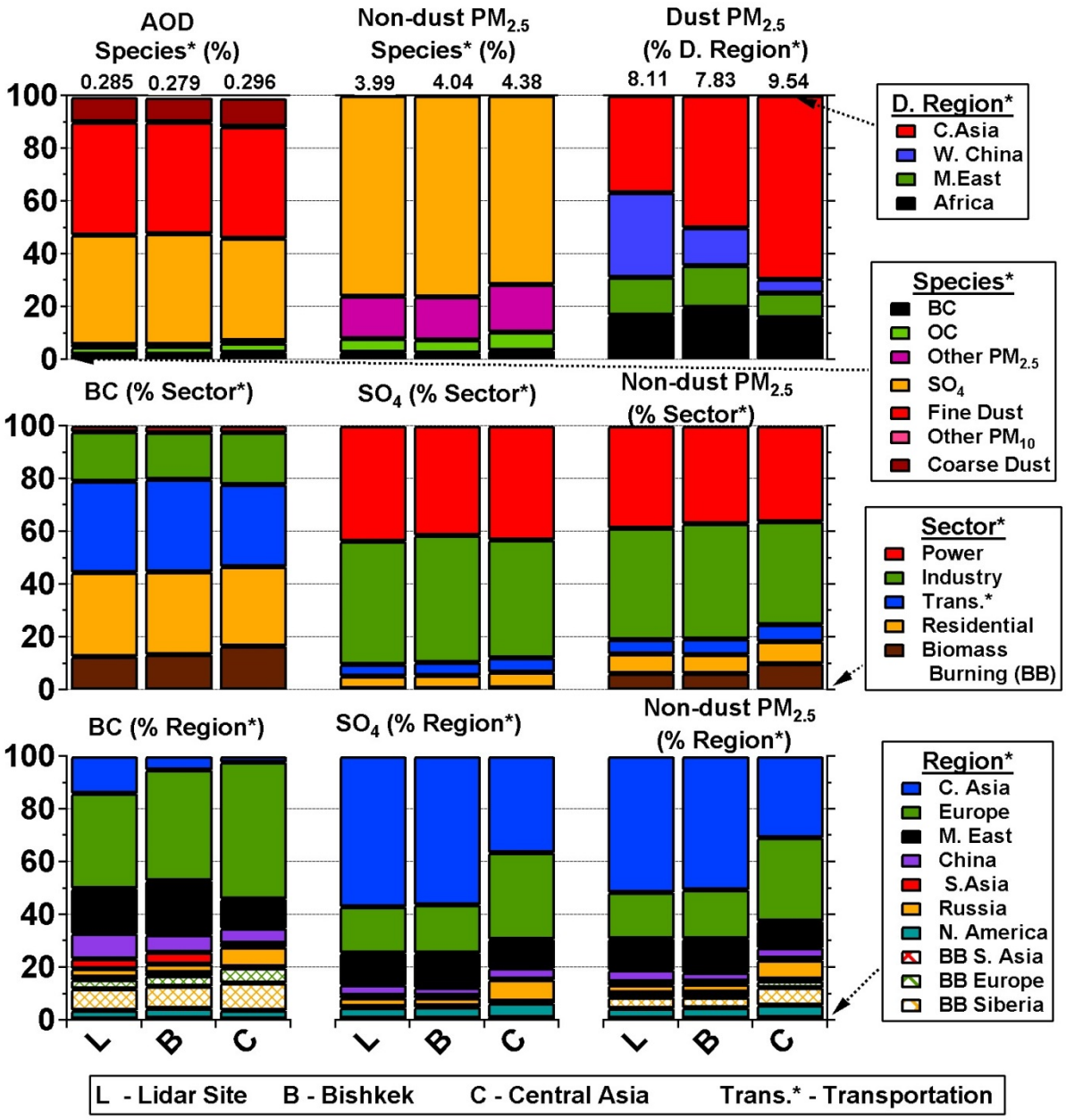

Fig. 7. Summary of period mean contributions by source regions and sectors for AOD, $PM_{2.5}$, dust, non-dust $PM_{2.5}$, sulfate and BC in % for the grid cells containing the Bishkek and LST observation sites, and spatially averaged over the Central Asia region. See Fig. 1 for anthropogenic, dust and fire source regions. Lidar denotes the LST (Lidar Station Teplokluchenka) site.

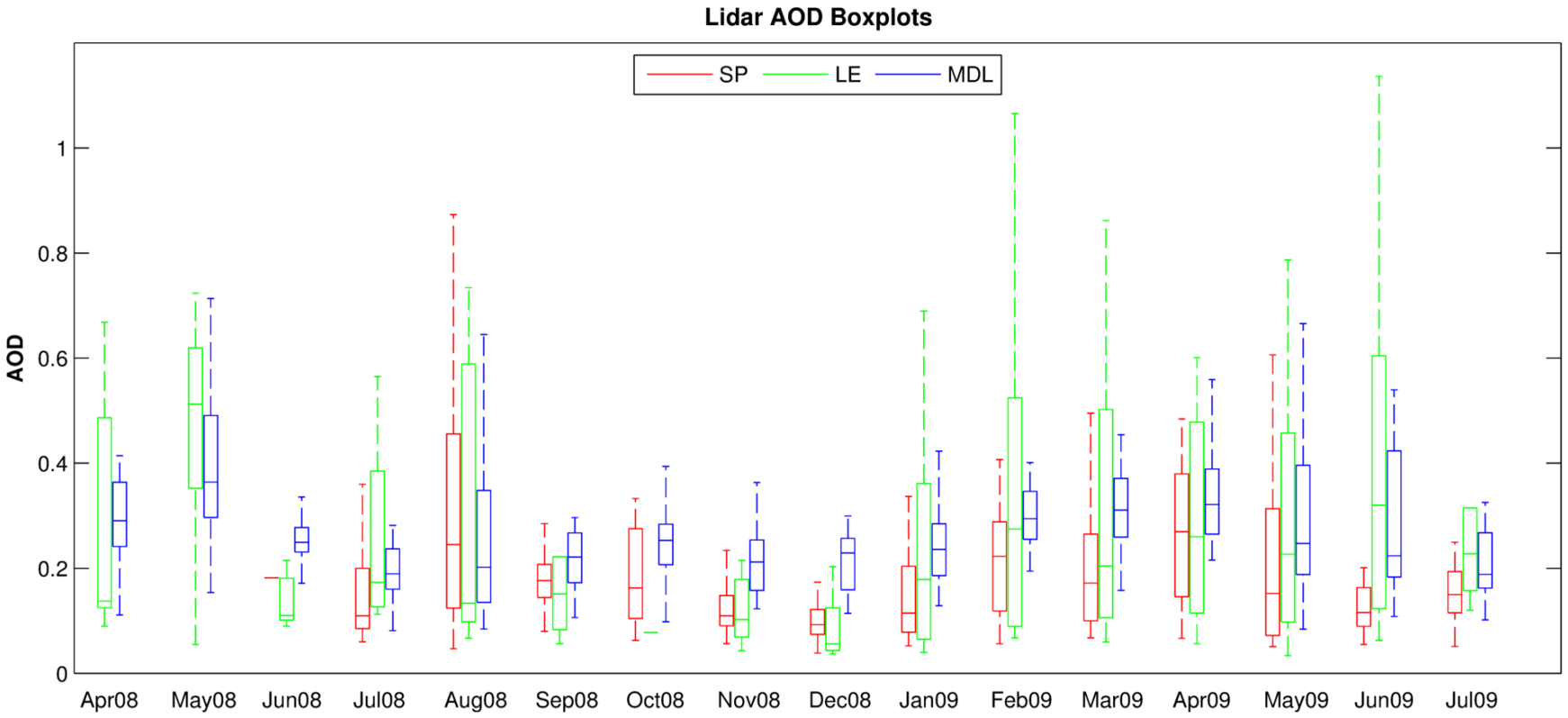

Fig. 8. Temporal variability in simulated AOD compared with observations at the LST site. The box-plots of monthly values are shown. AOD from the sun-photometer (SP) and integrated from the vertical extinction profiles (LE) are shown. MDL denotes modeled values. Lidar denotes the LST (Lidar Station Teplokluchenka) site. In each box whisker panel, the middle line denotes the median value, while the edges of the box represent 25th and 75th percentile values respectively. The whiskers denote the maximum and minimum values.

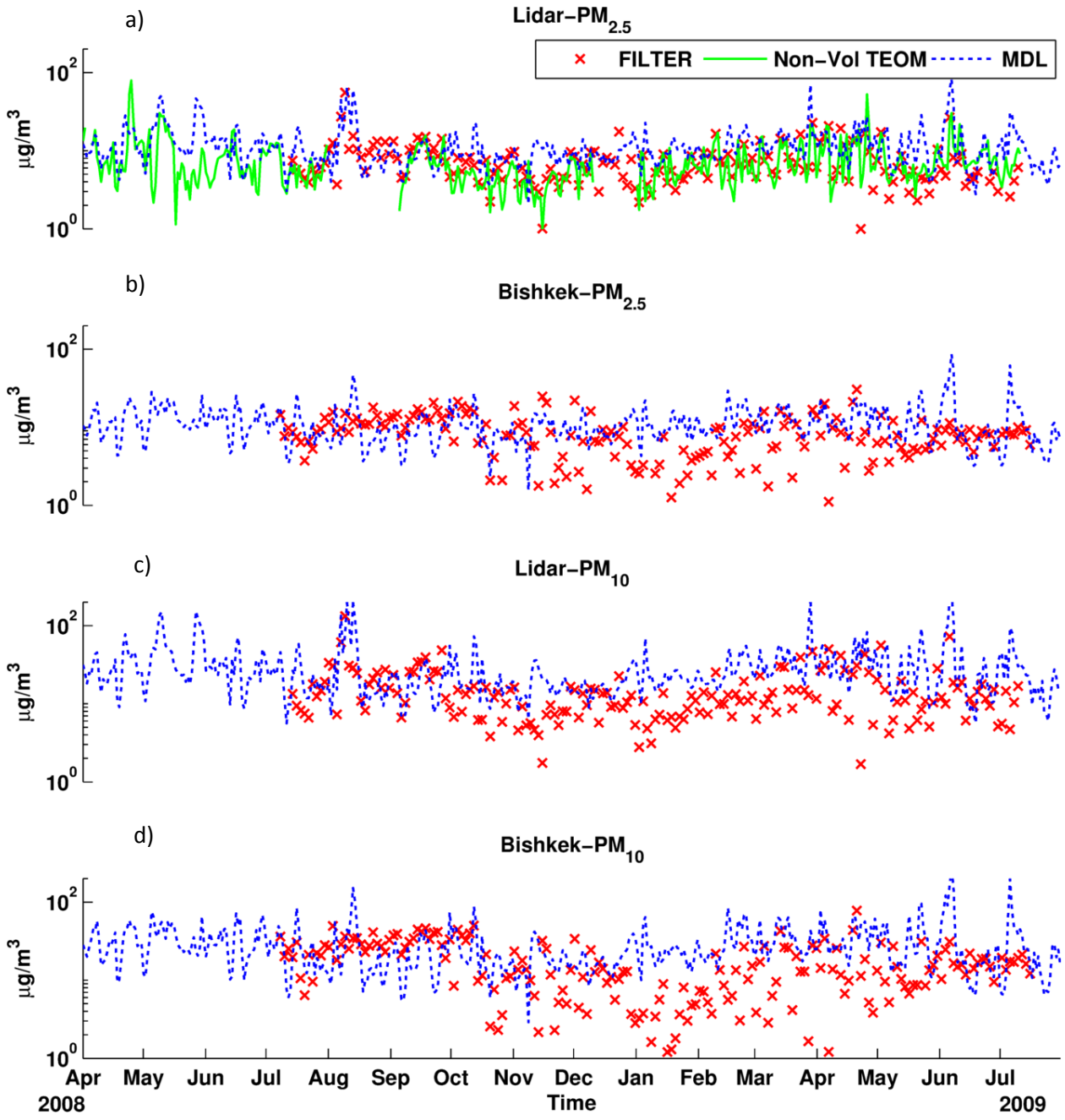

Fig. 9. Comparison of simulated PM mass with filter-based observations at Central Asia sites (a) $PM_{2.5}$ (LST) along with TEOM non-volatile measurements, (b) $PM_{2.5}$ (Bishkek), (c) PM_{10} (LST), and (d) PM_{10} (Bishkek) in (µg/m^3). Lidar denotes the LST (Lidar Station Teplokluchenka) site.

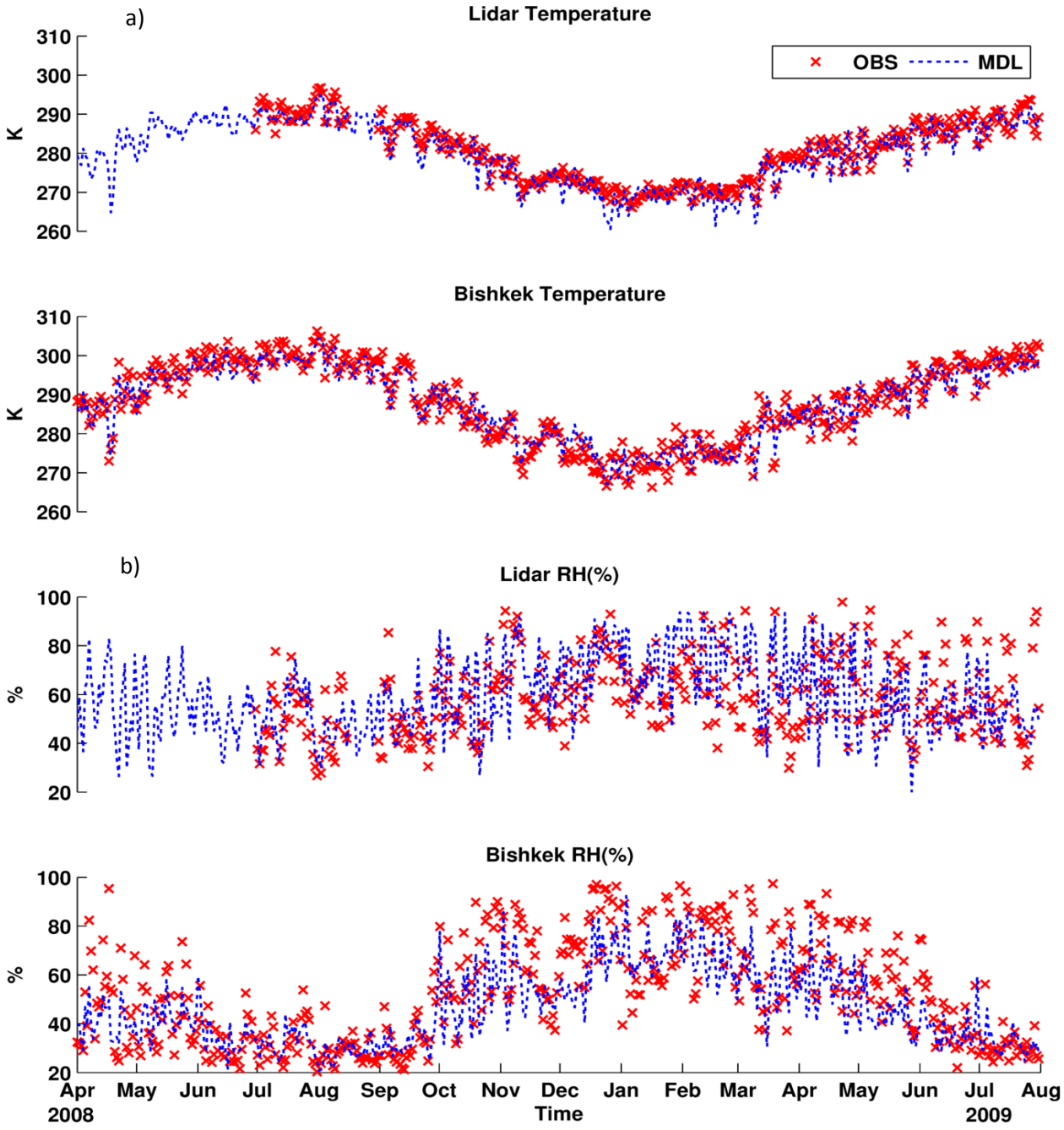

Fig. 10. Temporal variability in simulated Temperature (K) and (b) Relative Humidity RH (%) from WRF model compared with observations at the LST and Bishkek sites. Lidar denotes the LST (Lidar Station Teplokluchenka) site.

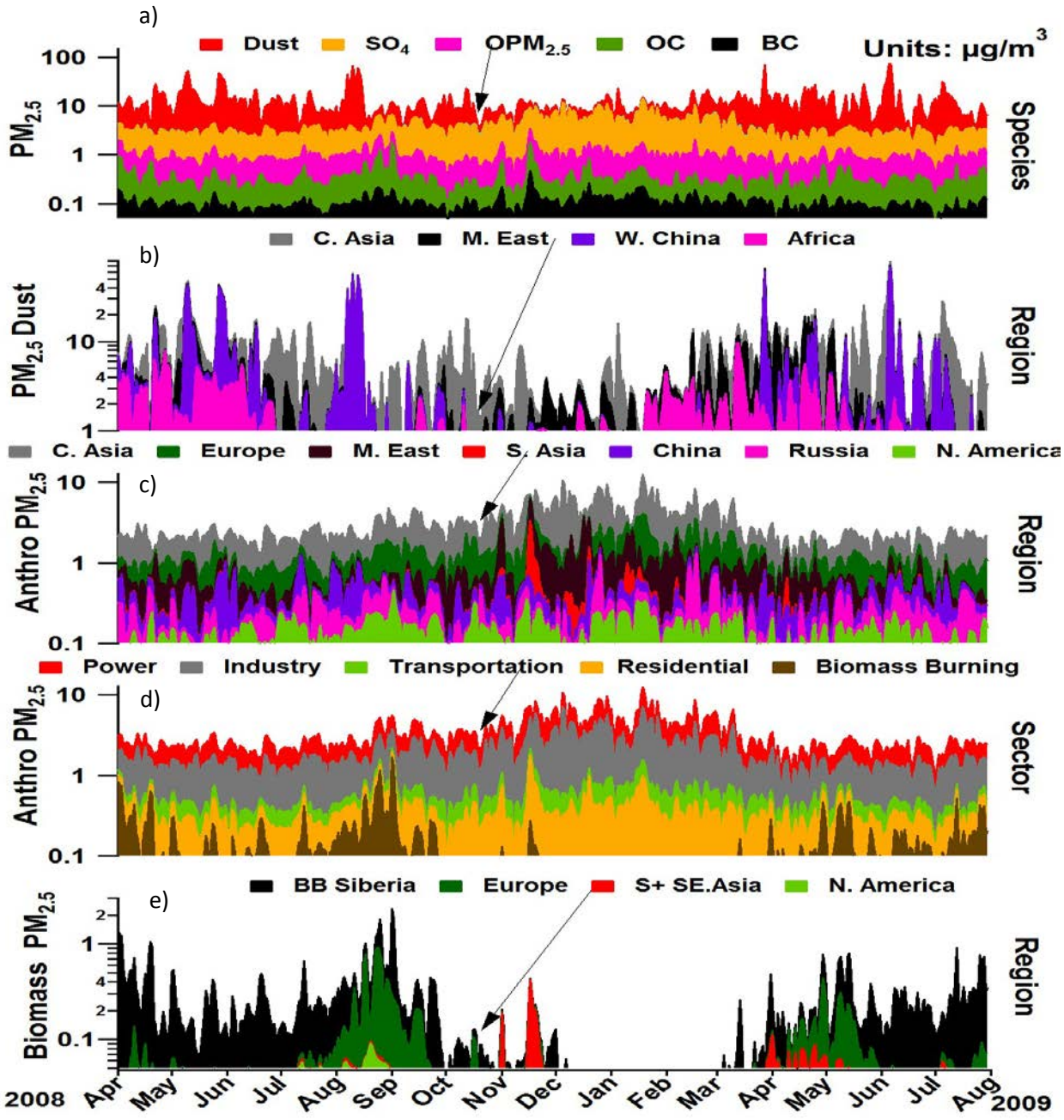

Fig. 11. Simulated composition of $PM_{2.5}$ at the LST site by a) Species (µg/m^3), b) Source sector (µg/m^3), and c) Source regions (µg/m^3). The contributions from source region and sectors denote the non – dust portion of $PM_{2.5}$ mass.

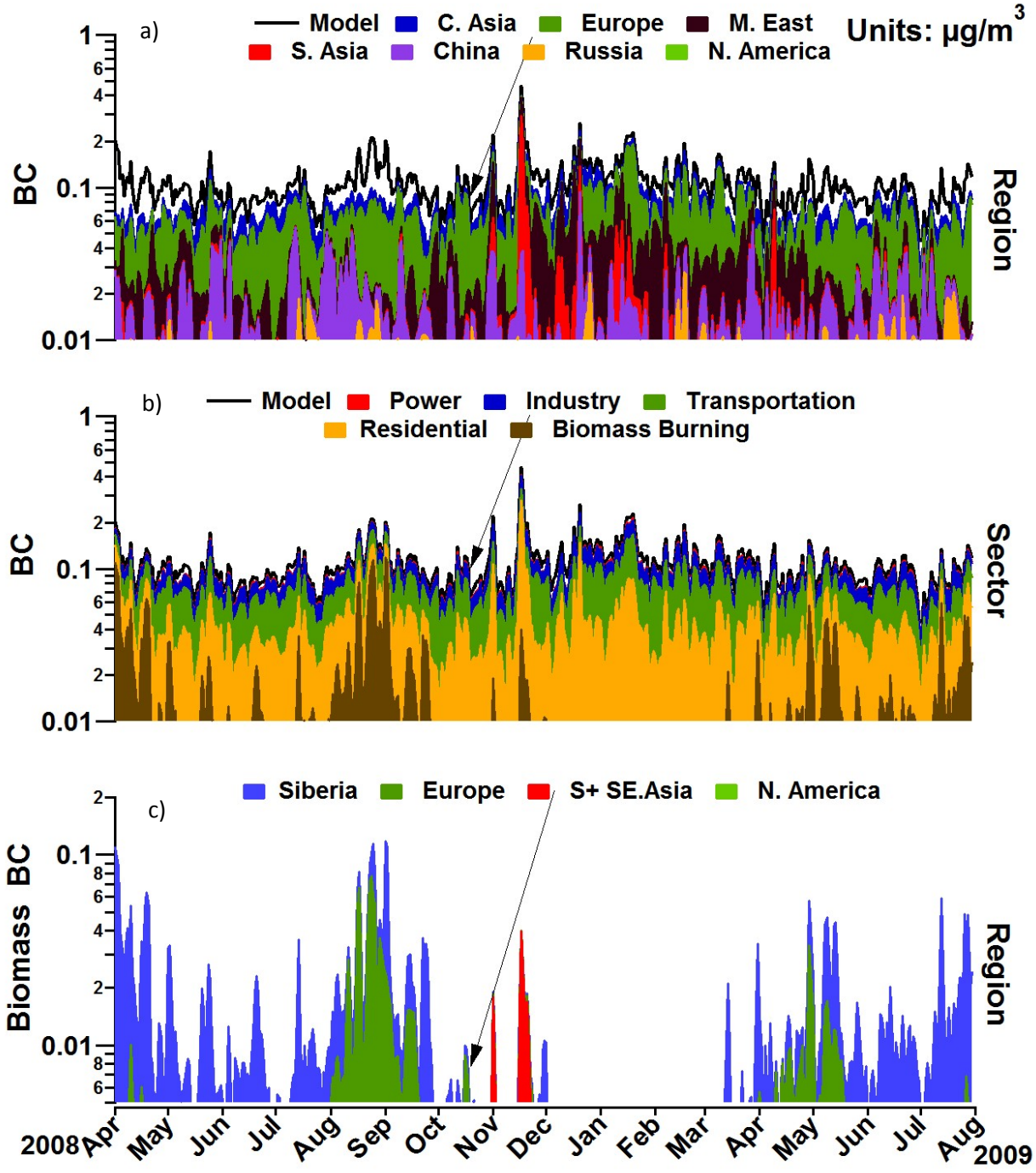

Fig. 12. Simulated composition of BC at the LST site by a) Source regions (µg/m^3), b) Source sector (µg/m^3), and c) Biomass burning source regions (µg/m^3).

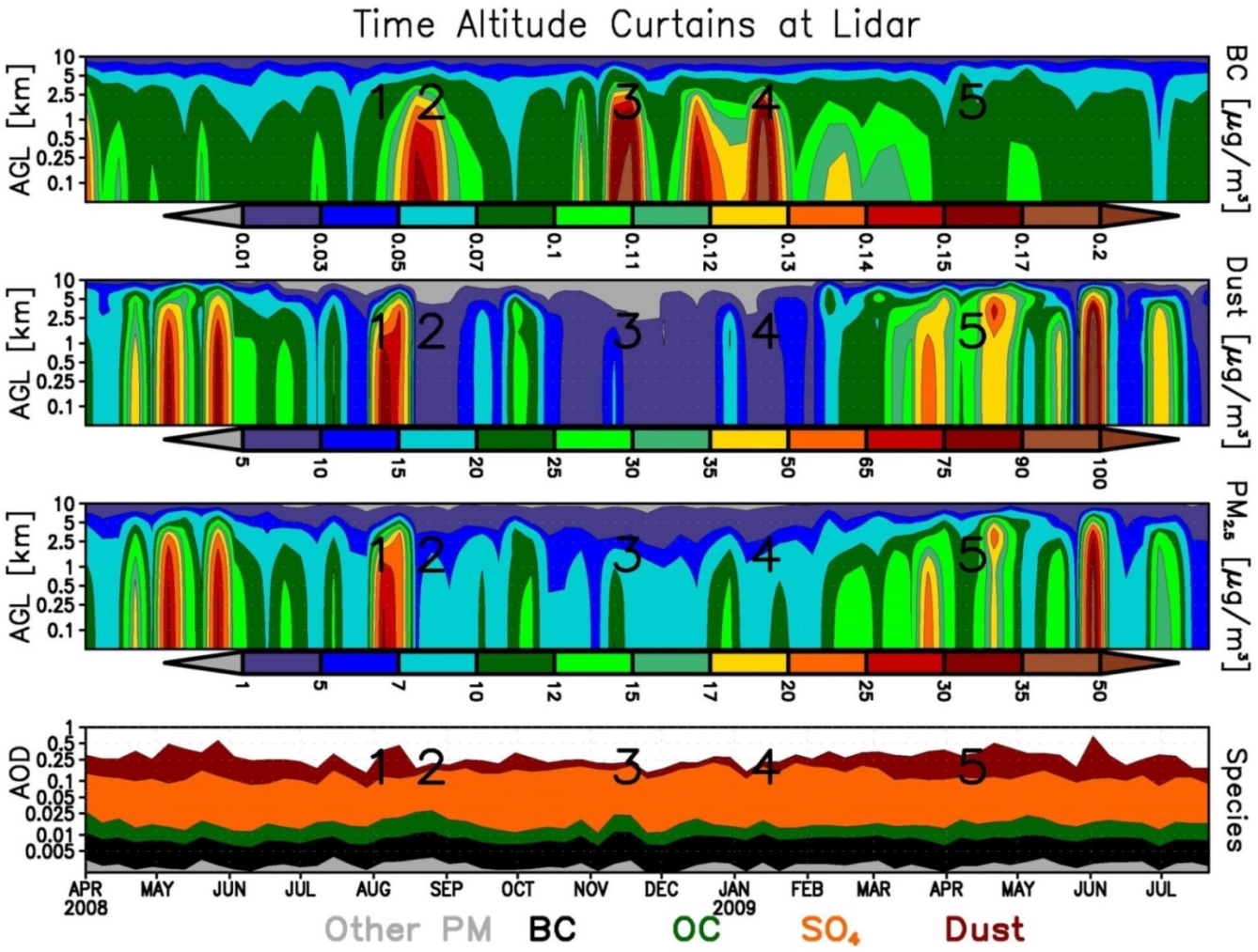

Fig. 13. Time altitude cross sections of weekly averaged predicted BC, dust and $PM_{2.5}$ for the simulation period at the LST site. The numbers denote the specific episodes of aerosol enhancements for back trajectory analysis in Fig. 14 and Fig. 15. Lidar denotes the LST (Lidar Station Teplokluchenka) site.

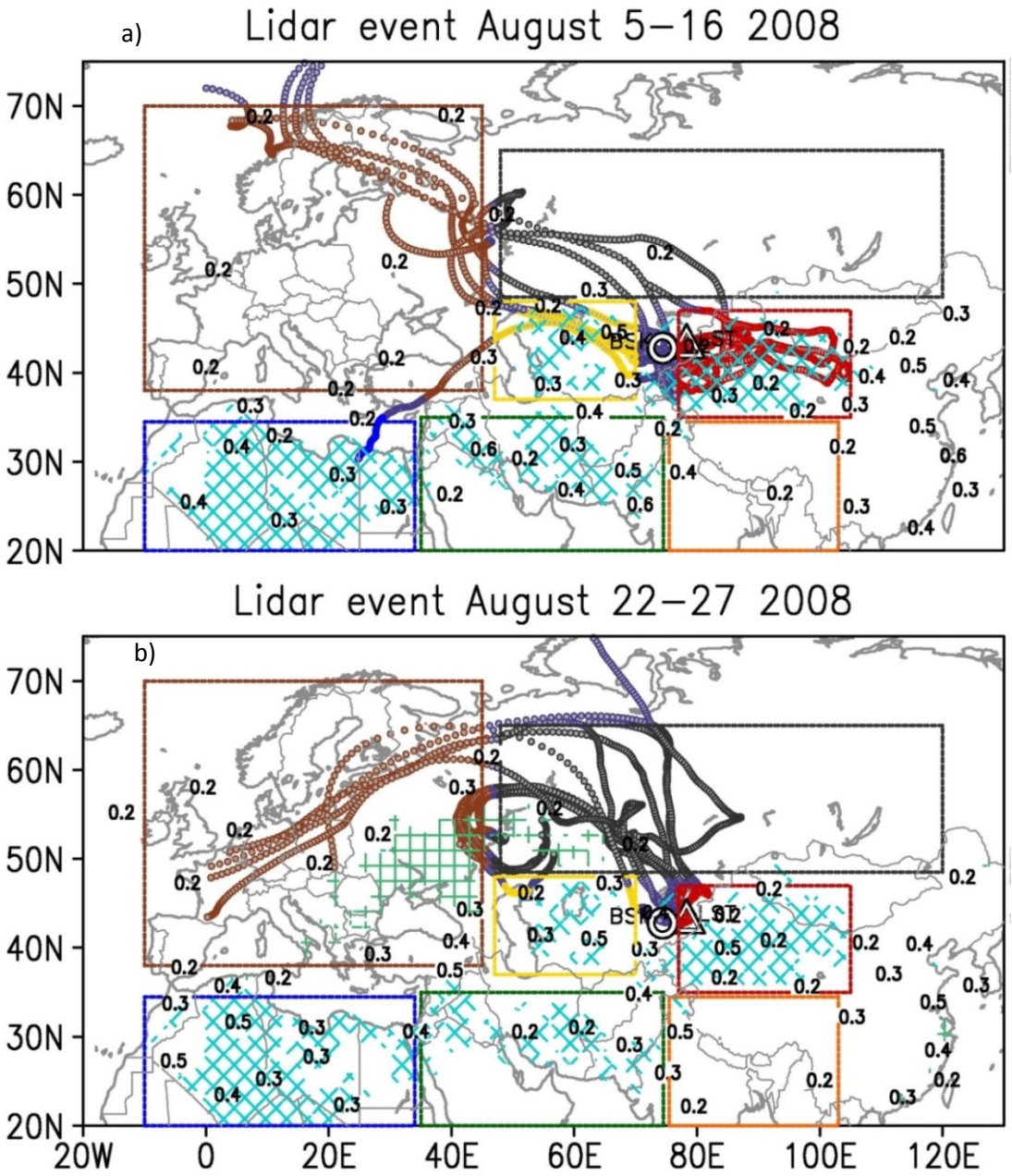

Fig. 14. Ten day air mass back trajectories for August 2008 (events 1 and 2 as denoted in Fig. 11) color coded by source regions. The blue diamond and green square hatched areas denote the natural dust and biomass burning emission sources while the number in black denote MODIS AOD contours averaged over the event time period and ten day prior time window. The trajectories are color coded by source regions including Africa (blue), Middle East (green), Central Asia (yellow), North Asia biomass (> 50° N, black), Europe (brown), China (red) and South Asia (orange). (green), Central Asia (yellow), North Asia biomass (> 50° N, black), Europe (brown), China (red) and South Asia (orange). Lidar denotes the LST (Lidar Station Teplokluchenka) site.

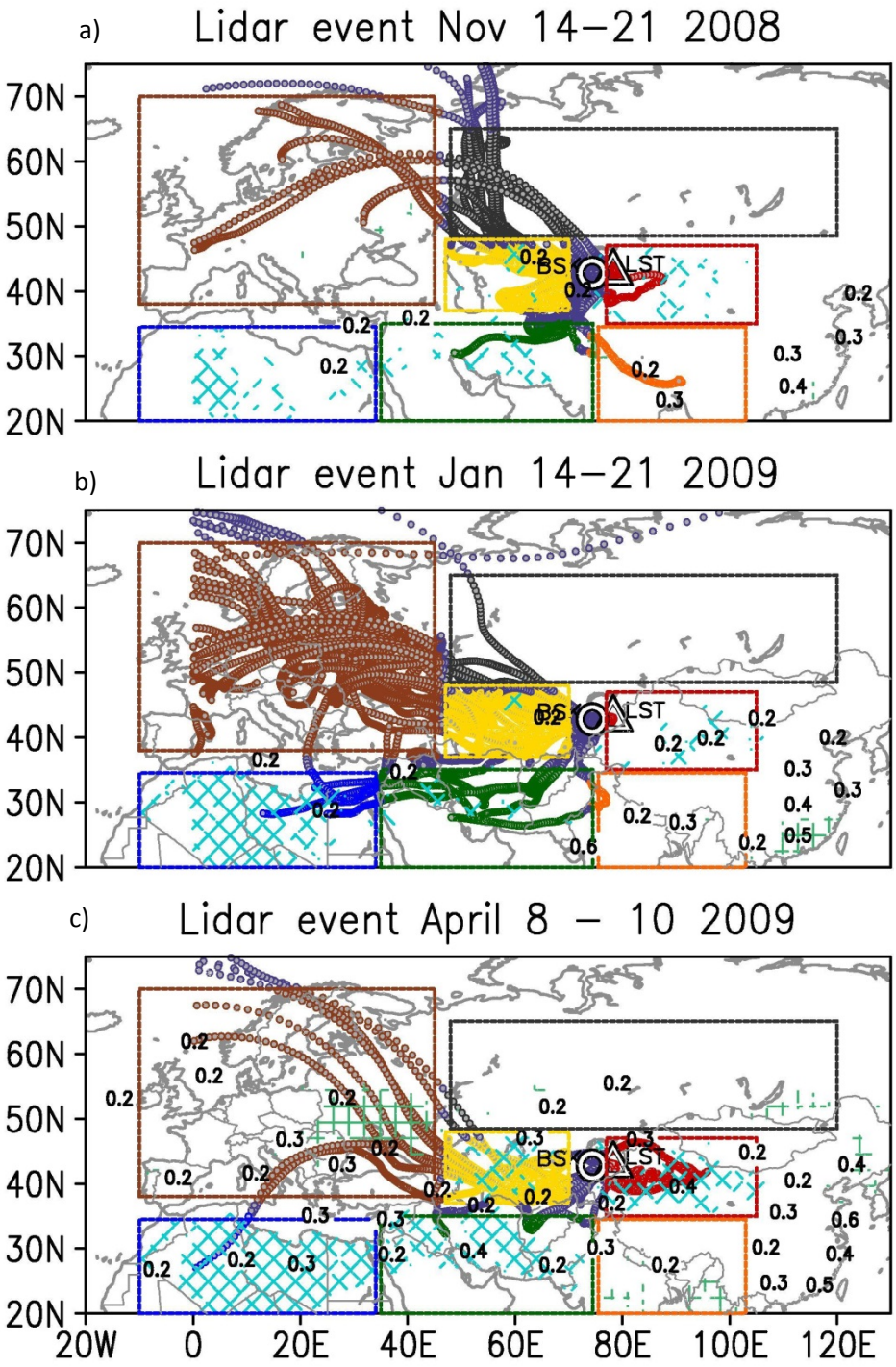

Fig. 15. Same as Fig. 14 but for November 2008, January 2009 and April 2009 (events 3, 4, 5 denoted in Fig. 13).

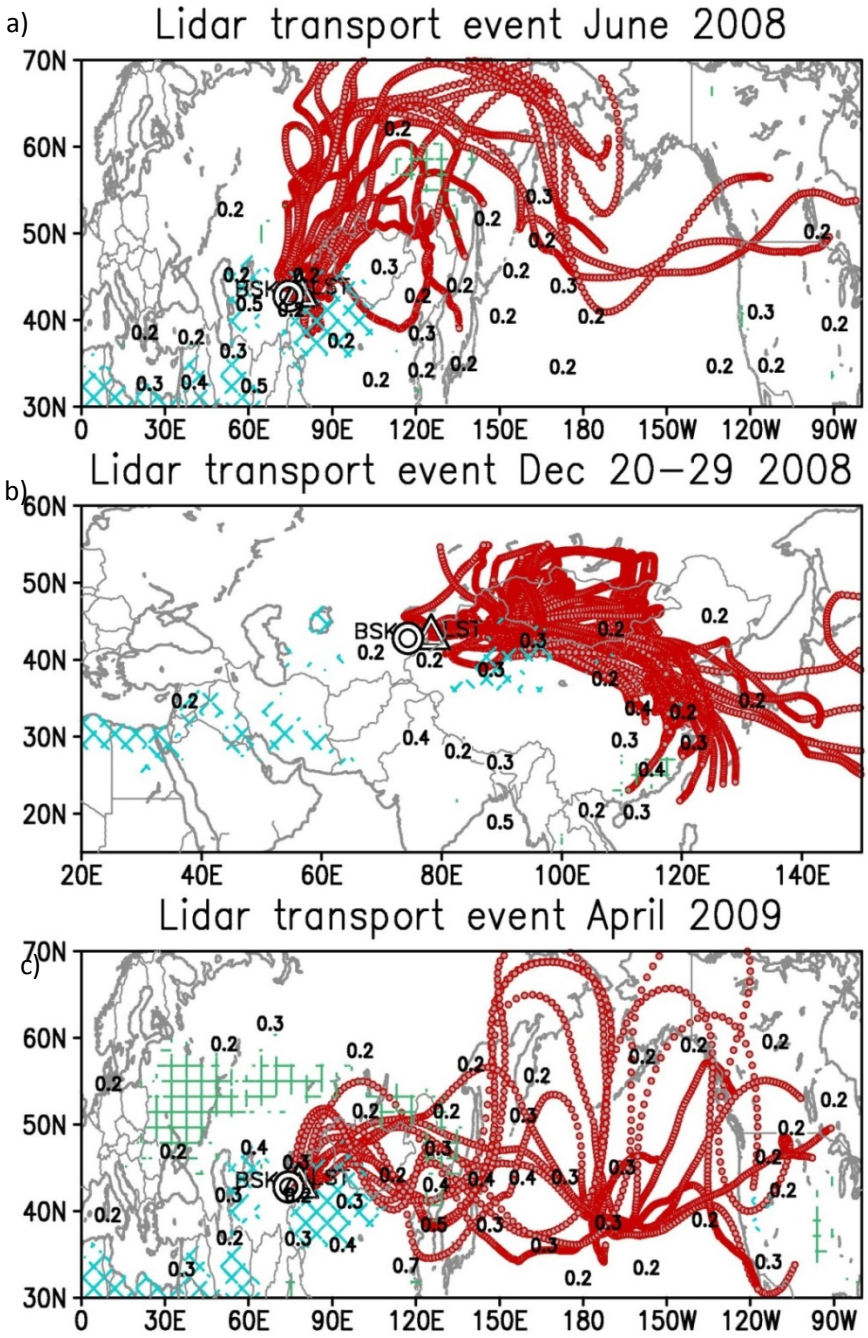

Fig. 16 Ten day air mass forward trajectories illustrating the seasonality in transport pathways out of CA for a) June 2008, b) December 2008, and c) April 2009. The blue diamond, green square hatched areas denote the natural dust and biomass burning emission sources while the number in black denote MODIS AOD contours, respectively, averaged over the event time period and subsequent ten day time window. Lidar denotes the LST (Lidar Station Teplokluchenka) site.

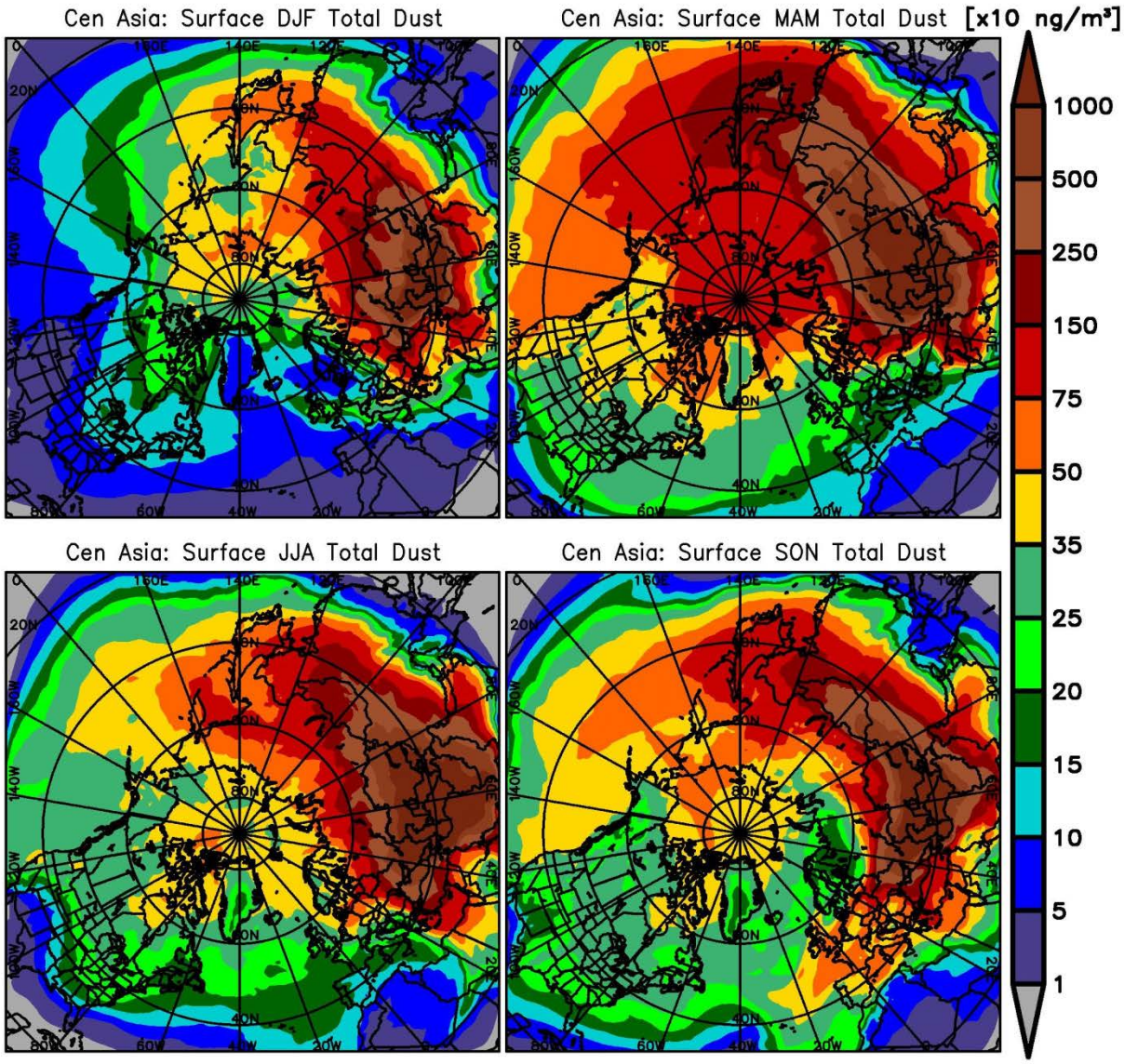

Fig. 17. Seasonally averaged surface total dust (PM_{10}) concentrations from Central Asia dust emissions. DJF (top left panel) denotes the average for the months of December, January and February. MAM (top right panel) denotes the average for months of March, April and May. JJA (bottom left panel) denotes the average for months of June, July and August while SON (bottom right panel) denotes average for months of September, October and November.

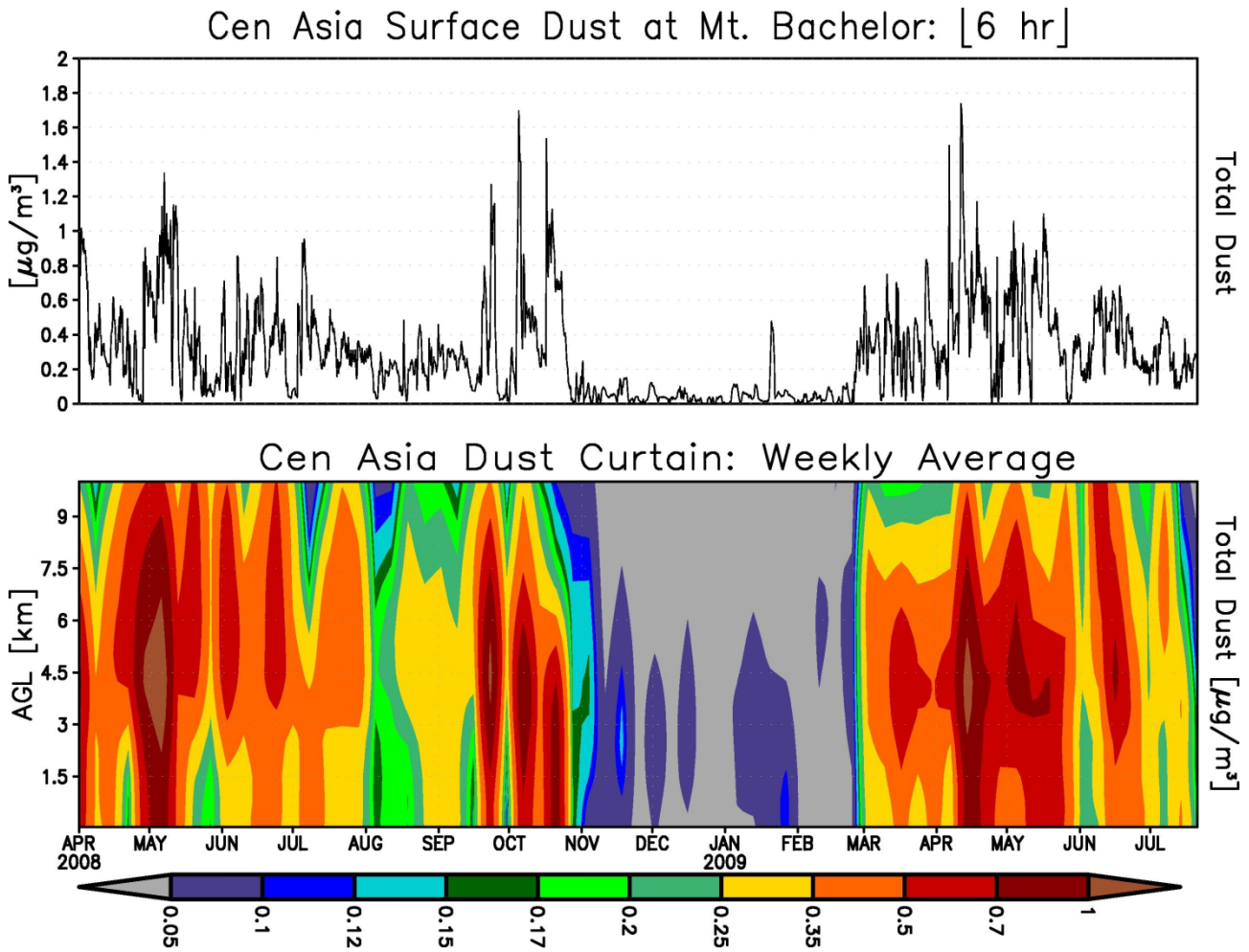

Fig. 18. Time series of predicted surface concentration at 6 h time step (top panel) and weekly averaged time altitude cross sections (bottom panel) of total dust (PM_{10}) from Central Asia dust emissions at Mt. Bachelor, Oregon.

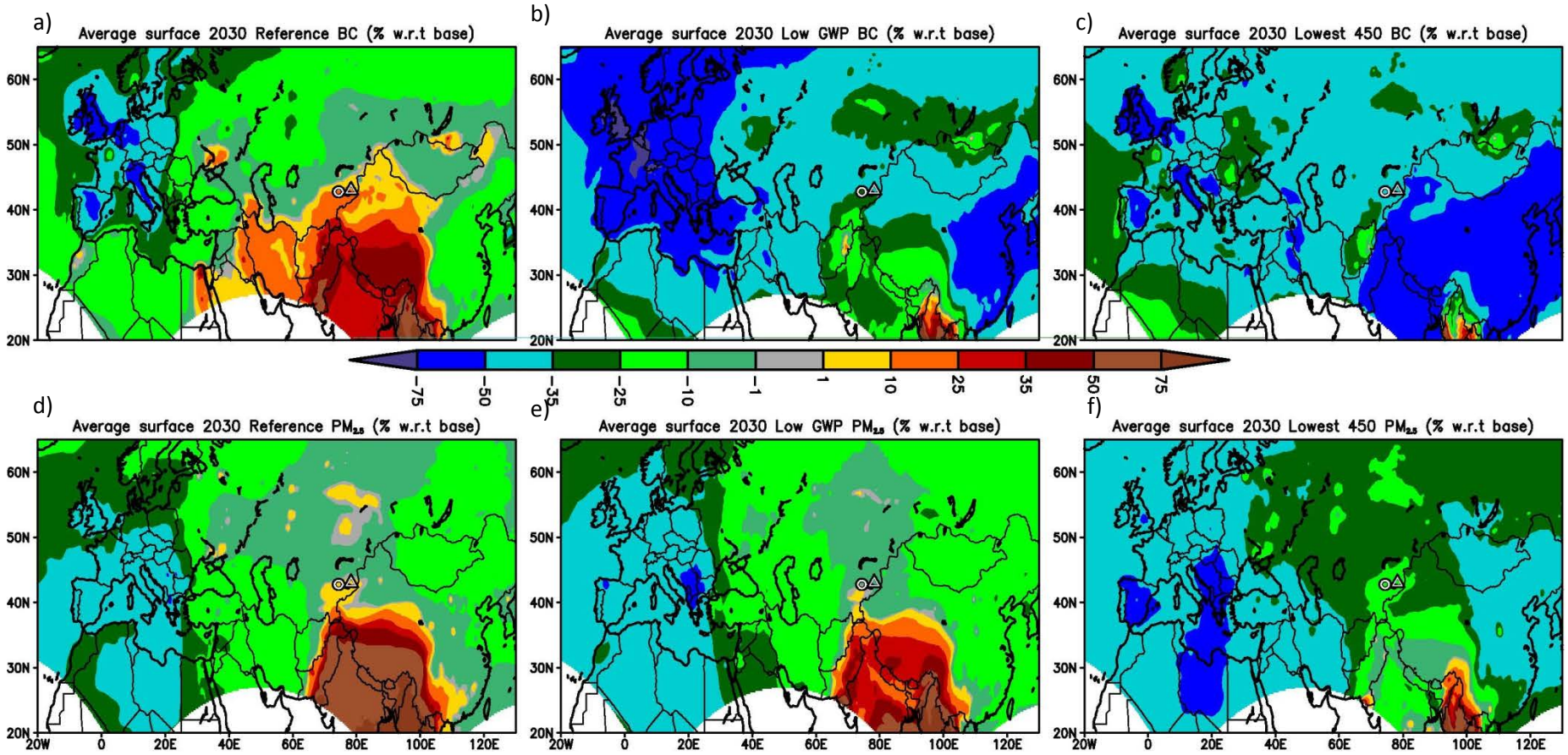

Fig. 19. Percent change in simulated period mean surface BC and $PM_{2.5}$ concentrations for future 2030 emission scenarios relative to the base year (2005) a),d) reference 2030, a),e) BC measures (low) and c),f) BC (lowest) and greenhouse gas measures aimed at keeping CO_2 levels below 450 ppm. Refer to Sec. 2.3 for more details on emission scenarios.